Article

Irritant-evoked activation and calcium modulation of the TRPA1 receptor

https://doi.org/10.1038/s41586-020-2480-9

Received: 13 January 2020

Accepted: 21 April 2020

Published online: 08 July 2020

Check for updates

Jianhua Zhao[1,5], John V. Lin King[2,3,5], Candice E. Paulsen[2,4], Yifan Cheng[1]✉ & David Julius[2]✉

The transient receptor potential ion channel TRPA1 is expressed by primary afferent nerve fibres, in which it functions as a low-threshold sensor for structurally diverse electrophilic irritants, including small volatile environmental toxicants and endogenous algogenic lipids[1]. TRPA1 is also a 'receptor-operated' channel whose activation downstream of metabotropic receptors elicits inflammatory pain or itch, making it an attractive target for novel analgesic therapies[2]. However, the mechanisms by which TRPA1 recognizes and responds to electrophiles or cytoplasmic second messengers remain unknown. Here we use strutural studies and electrophysiology to show that electrophiles act through a two-step process in which modification of a highly reactive cysteine residue (C621) promotes reorientation of a cytoplasmic loop to enhance nucleophilicity and modification of a nearby cysteine (C665), thereby stabilizing the loop in an activating configuration. These actions modulate two restrictions controlling ion permeation, including widening of the selectivity filter to enhance calcium permeability and opening of a canonical gate at the cytoplasmic end of the pore. We propose a model to explain functional coupling between electrophile action and these control points. We also characterize a calcium-binding pocket that is highly conserved across TRP channel subtypes and accounts for all aspects of calcium-dependent TRPA1 regulation, including potentiation, desensitization and activation by metabotropic receptors. These findings provide a structural framework for understanding how a broad-spectrum irritant receptor is controlled by endogenous and exogenous agents that elicit or exacerbate pain and itch.

Electrophiles activate TRPA1 through covalent modification of cysteine residues within the channel's cytoplasmic amino terminus[3–5]. We have previously shown that three critical cysteines (C621, C641 and C665 in human TRPA1) reside in an intricately folded region situated just below the transmembrane core of the channel[6]. This and a more recent structural study[7] suggest that the local chemical environment within this 'allosteric nexus' endows C621 with a highly nucleophilic character that probably accounts for the channel's low threshold sensitivity[5]. But how this clamshell-shaped region accommodates small and large electrophiles and translates local conformational changes into gating movements remains largely unknown[7]. TRPA1 is also activated by G-protein-coupled or growth factor receptors that stimulate phospholipase C signalling pathways[8–11], but the contribution of relevant second messengers, such as cytoplasmic calcium or phosphoinositide lipids, and their sites of action remain controversial[12]. Moreover, TRPA1 exhibits bimodal modulation by calcium—which first potentiates then desensitizes electrophile-evoked responses[8,13]—for which several mechanisms have been proposed[13–17]. Here we clarify these key questions from a structural perspective.

Dynamic equilibrium between two states

TRPA1 exhibits 'flickery' behaviour characterized by rapid transitions between open and closed states (Fig. 1a, Extended Data Fig. 1a), but a pharmacologically validated open state has not yet been visualized[6,7]. Two technical insights enabled us to overcome this limitation. First, extraction with CYMAL-5 neopentyl glycol (NG) detergent yielded a stable distribution of two main conformations (Fig. 1 a, b, Extended Data Fig. 2, Extended Data Table 1). We then used pharmacological agents to validate these as open and closed states. One conformation bound the antagonist A-967079 (A-96), showed a narrow pore profile, and resembles previously published structures; we designated this conformation as closed. Second, we found that treating TRPA1-expressing cells with an irreversible electrophilic agonist (iodoacetamide, IA) before detergent extraction biased the equilibrium towards the other main conformation, which showed IA modification of C621 and a wider pore profile, pharmacologically validating it as an activated, open state.

Comparison of these two states revealed substantial conformational differences within the transmembrane core and membrane-proximal

[1]Department of Biochemistry and Biophysics and Howard Hughes Medical Institute, University of California, San Francisco, San Francisco, CA, USA. [2]Department of Physiology, University of California, San Francisco, San Francisco, CA, USA. [3]Neuroscience Graduate Program, University of California, San Francisco, San Francisco, CA, USA. [4]Present address: Department of Molecular Biophysics and Biochemistry, Yale School of Medicine, New Haven, CT, USA. [5]These authors contributed equally to this work: Jianhua Zhao, John V. Lin King. ✉e-mail: yifan.cheng@ucsf.edu; david.julius@ucsf.edu

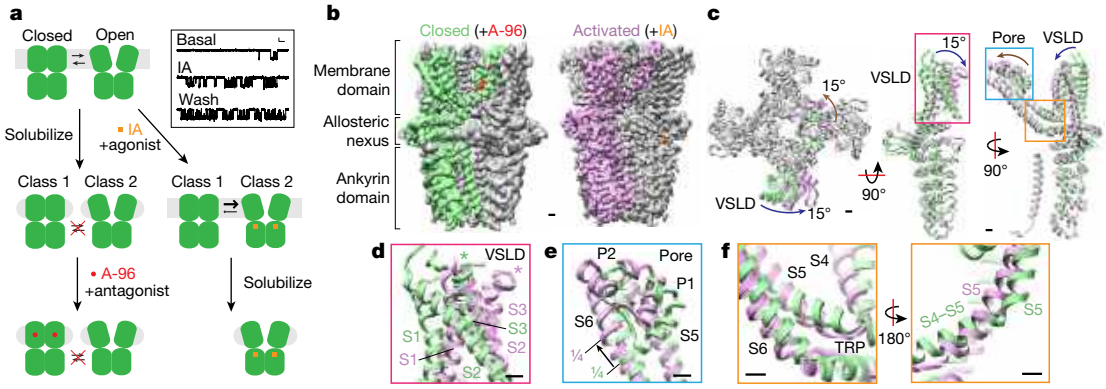

Fig. 1 | Dynamic equilibrium between closed and activated conformations. **a**, Closed and open states of TRPA1 were captured by incubation with an irreversible electrophilic agonist (IA) or an antagonist (A-96) before or after membrane solubilization, respectively. Representative inside-out patch recordings show spontaneous (basal) and IA (100 μM)-evoked (persistent) TRPA1 channel openings (holding voltage (V_{hold}) = −40 mV; scale bars, 10 ms (*x*), 2 pA (*y*); *n* = 9 independent experiments). **b**, Cryo-electron microscopy density maps of TRPA1 bound to A-96 or IA in closed or activated state, respectively. A-96 binds to the membrane domain, whereas iodoacetamide binds to the allosteric nexus. **c**, Comparison between subunits in closed and activated conformations showing about 15° rotation of the voltage sensor-like domain (VSLD) and twisting and translation of the pore domain. The ankyrin-repeat domain remains stationary. **d**, The VSLD rotates around the cytoplasmic base of transmembrane α-helices S1 and S2 in a near-rigid-body movement. **e**, The pore domain twists and translates upward towards the extracellular milieu, concomitant with a shift in the S6 π-helix by one helical turn. **f**, Conformational changes in the upper pore region are coupled to widening of the lower gate through straightening of the S5 α-helix, enabling movement of S6 to facilitate gating. Scale bars (**b**–**f**), 10 Å.

allosteric nexus (Fig. 1c–f, Supplementary Video 1). In the activated state, the entire transmembrane region rotates by approximately 15° relative to the stationary cytoplasmic ankyrin-repeat domain (Fig. 1c). Moreover, the voltage sensor-like domain undergoes a near-rigid-body rotation (Fig. 1d), which is accompanied by rotation and upward translation of the pore loop and pore helices (Fig. 1e). These transitions are linked by movements in the S5 and S6 helices: the π-helix in S6 shifts up by one helical turn and, in concert with S5, causes an upward shift of pore helices P1 and P2 (Fig. 1e); the S4–S5 linker and S5 transmembrane α-helix straighten into a single α-helix (Fig. 1f), which coordinates movement of the pore helices and S6 to couple the upper and lower gates. In sum, these transitions are reminiscent of those seen between closed and desensitised states for the cold and menthol receptor TRPM8, but dissimilar to the more local conformational changes that accompany gating of the heat and capsaicin receptor TRPV1[18,19].

Coupling between upper and lower gates

Profiles of the ion-permeation pathway revealed substantial changes at both upper and lower restrictions (Fig. 2a, b). We observed marked widening of the lower gate formed by residues I957 and V961, dilating the pore diameter from 5.3 to 7.8 Å (Fig. 2c) and increasing its hydrated radius from 0.9 to 2.1 Å (Fig. 2b). These changes are nearly identical to those seen in TRPV1 when comparing apo and capsaicin-activated states, indicative of transition from closed to open, as expected for a true gate that controls ion flux[19]. Local resolution analysis of the activated TRPA1 map shows that the lower gate has slightly diminished resolution compared with surrounding regions (Extended Data Fig. 2e), suggesting a dynamic profile that is consistent with the channel's ability to pass cations of different sizes[20,21].

At the upper restriction, movement of pore helices P1 and P2 results in an upward shift and dilation of the selectivity filter formed by residues G914 and D915 (Fig. 2a, b). This alters the overall profile of the outer pore wall from a V- to a U-shaped funnel, which increases the restriction diameter from 8.5 to 9.7 Å (Fig. 2d). Of note, widening of both upper and lower restrictions is elicited by electrophile attachment to the allosteric nexus, below the transmembrane core, arguing for allosteric coupling between this nexus and both gates. Regarding communication between the gates, we noted that S5 contains a small bend that straightens upon transition to the open state (Fig. 1f), consequently lifting and rotating the pore helices backward to alter configuration of the selectivity filter (Fig. 2a). Consistent with these proposed coupling movements, the A-96 antagonist wedges into a pocket near the S5 bend and just beneath the pore helices (Extended Data Figs. 1e, 9a–c), as previously described[6]. Thus, A-96 probably prevents opening of the lower gate by locking S5 in its closed (bent) conformation and inhibiting movement of the S5–S6 pore module (Extended Data Fig. 9d, g).

What might be the physiological relevance of such movements in the outer pore region, which alter diameter less compared with TRPV1? Notably, this transition involves upward and outward rotation of D915 (Fig. 2b, d), a residue that influences calcium selectivity of activated TRPA1 channels[13,22]. Increased negative electrostatic surface potential in the outer pore region (Fig. 2d) is consistent with enhanced calcium preference of the activated state[13,20,21,23]. Indeed, neither D915A nor D915N mutants exhibit preference for calcium[13], and models of these mutants show reduced negative electrostatic surface potential in the activated state (Extended Data Fig. 3). Together, these observations support the notion that conformational transitions at the level of the selectivity filter account for dynamic ion selectivity of TRPA1[13,20,21,23].

Two-step mechanism of electrophile action

Our activated TRPA1 structure was obtained using IA, which functions as an irreversible agonist by forming stable covalent adducts with cysteine residues[3,4] (Fig. 1a, Extended Data Fig. 1a). We observed clear attachment of IA at just one position, C621 (Extended Data Fig. 4a), consistent with the exceptional nucleophilic character of this residue[5,6]. This modification also stabilized an activation loop (A-loop) in an upward configuration, exposing a pocket containing the modified residue (Fig. 3a, b, Extended Data Fig. 4a, d), consistent with recently reported structures of the electrophile-modified channel[7].

To better visualize agonist attachment, we used a bulky version of IA (BODIPY–IA (BIA)) (Extended Data Fig. 1e) and solubilized ligand-free and BIA-modified channels with the detergent lauryl maltose neopentyl glycol (LMNG), which resulted in higher overall resolutions of 3.1 and 2.6 Å, respectively (Extended Data Figs. 2, 4c, Extended Data Table 1). While these channels were both trapped in a closed pore state, covalent modification and distinct A-loop conformations could be more clearly observed (Fig. 3a, b). The downward (ligand-free) A-loop, which was not previously visualized[7], occluded the reactive pocket

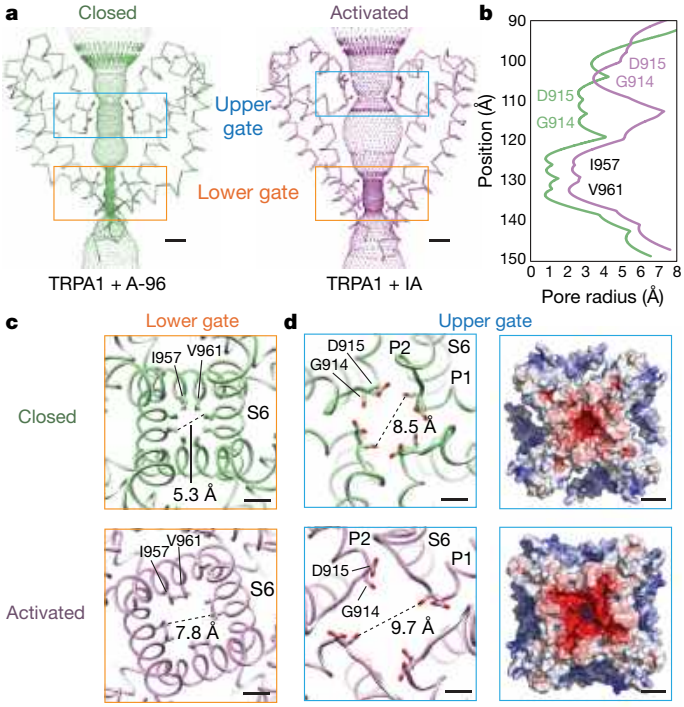

Fig. 2 | Coupled dilation of upper pore region and lower gate. a, Activation of TRPA1 involves concerted dilation of both upper and lower gates with upward shift of the selectivity filter. **b**, The lower gate is formed by residues I957 and V961, while the upper gate is formed by D915 and the backbone carbonyl of G914. **c**, Pore widening is associated with anticlockwise rotation of transmembrane α-helices (viewed from extracellular face to cytoplasmic side). **d**, Acidic residues lining the upper pore create a highly negatively charged surface, especially in the activated conformation, probably facilitating calcium selectivity. Scale bars, 5 Å. Electrostatic surface charge distributions of the cytoplasmic face of TRPA1 in apo- and activated states were calculated in APBS[33] and displayed at ±10 kT e^{-1}. Scale bars, 25 Å.

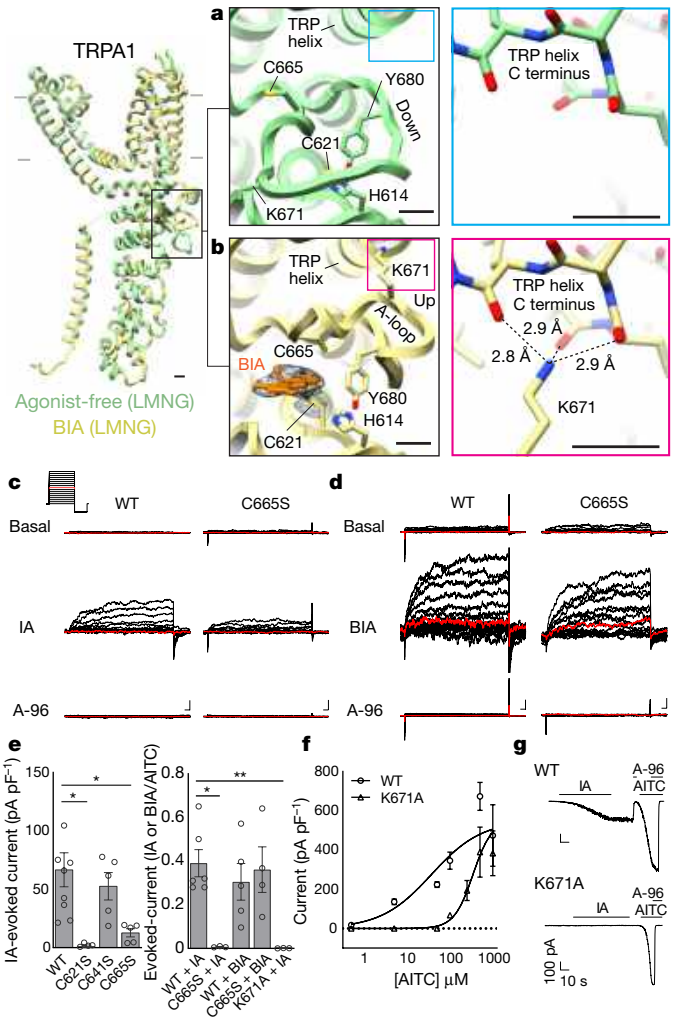

Fig. 3 | Activation by electrophiles occurs through a two-step mechanism. **a**, A dynamic activation loop (A-loop) adopts a 'down' conformation in the agonist-free channel, partially occluding a reactive pocket containing C621. **b**, Following attachment of BIA to C621, the A-loop transitions to an 'up' conformation, bringing C665 into the reactive pocket and repositioning K671 to coordinate backbone carbonyl oxygens at the TRP domain C terminus. Scale bars, 5 Å. **c**, IA (100 µM)-evoked currents for wild-type (WT) and C665S-mutant TRPA1 channels ($n = 9$ and 5 independent experiments, respectively), followed by inhibition with A-96 (10 µM). **d**, As **c**, but for BIA (100 µM)-evoked currents ($n = 5$ for wild type and C665S mutant); 500 ms voltage steps from −80 to +80 mV, 0 mV coloured red. Scale bars, 25 ms (x), 100 pA (y). **e**, Left, quantification of IA-evoked currents for wild-type or mutant TRPA1 channels at 80 mV ($n = 9$ and 5 independent experiments per construct, respectively). Right, normalized IA-evoked currents (wild type, $n = 6$; C665S, $n = 3$; K671A, $n = 3$) and BIA-evoked currents (wild type, $n = 5$; C665S, $n = 4$). $^*P = 0.05$, $^{**}P = 0.007$; Kruskal–Wallis test with post hoc Dunn's correction for multiple comparisons. Data are mean ± s.e.m. **f**, AITC dose–response curves for wild-type ($EC_{50} = 37$ nM; 95% CI, 30–46 nM) and K671A ($EC_{50} = 344$ nM; 95% CI, 313–381 nM) TRPA1 channels. EC_{50} values determined by nonlinear Poisson regression and statistically significant difference confirmed with extra sum-of-squares F test ($P < 0.0001$). $n = 3$ cells per dose per construct except K671A 50 mM ($n = 6$) and 100 mM ($n = 4$). Data are mean ± s.e.m. **g**, IA (100 µM)- and AITC (1 mM)-evoked whole-cell currents for wild-type and K671A channels ($V_{hold} = -80$ mV) blocked by A-96 (10 µM). $n = 3$ independent experiments per construct.

containing C621 and C665 (Fig. 3a, Extended Data Fig. 4d), whereas the upward (electrophile-modified) conformation exposed this pocket. Furthermore, the larger density of BIA confirmed C621 as the primary modification site (Fig. 3b, Extended Data Fig. 4b). Other cysteines within this region (most notably C665) are also modified, but at substantially reduced rates compared to C621[5]. Indeed, in the presence of IA we observed a weaker density associated with C665, which may reflect partial modification at this site (Extended Data Fig. 4a), as also observed with benzyl isothiocyanate[7].

The role for C665 in TRPA1 activation has been unclear[5,7]. We observed that C665 rotates into the pocket containing modified C621 when the A-loop is stabilized in the upward configuration (Fig. 3a, b). This reorientation of C665 is predicted to lower its acid dissociation constant (pK_a) from 11.2 to 8.8 and enhance nucleophilicity (Extended Data Fig. 5h), suggesting that modification at this site also occurs during channel activation. The necessity for modification at one or both cysteines may depend on the size or charge of electrophile modification and whether it sufficiently alters configuration of the reactive pocket. To test this idea, we mutated cysteines (C621, C641 and/or C665) in the vicinity of the reactive pocket and used patch-clamp recording to assess their sensitivity to IA and BODIPY–IA. All double mutant combinations were IA insensitive (Extended Data Fig. 5b–d), demonstrating that C621 alone is insufficient to support channel activation by this small electrophile—even though C621 was fully labelled by BODIPY–IA in C641S/C665S double mutants (Extended Data Fig. 5g). We next examined single cysteine substitutions and found that TRPA1(C641S) behaved similarly to wild-type channels (Fig. 3e, Extended Data Fig. 5f), whereas TRPA1(C621S) was IA insensitive (Fig. 3e, Extended Data Fig. 5e) and TRPA1(C665S) retained about 30% sensitivity (Fig. 3c, e). This is consistent with a two-step model whereby C621 is the primary site of electrophile modification, priming A-loop reorientation and modification of C665 to elicit full channel activation. Suo et al. concluded that C665 modification is not required for channel activation[7], perhaps

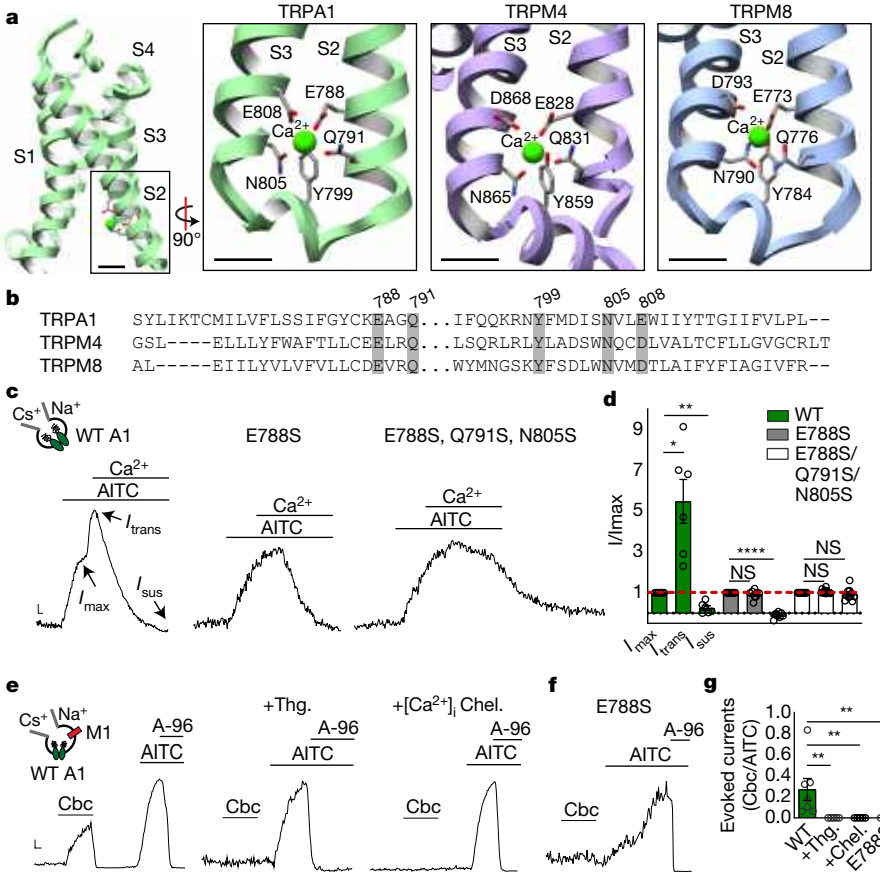

Fig. 4 | Three distinct modes of calcium regulation from one site. a, A calcium ion binds at the cytoplasmic end of S2–S3 helices in the voltage sensor-like domain, as seen in TRPM4 and TRPM8. Scale bars, 5 Å. **b**, Sequence alignment reveals conservation of calcium-coordinating residues in human TRPA1, human TRPM4 and avian TRPM8. **c**, Normalized whole-cell currents from wild-type ($n = 6$ independent experiments), E788S ($n = 8$) and E788S/Q791S/N80S triple-mutant ($n = 10$) TRPA1 following bath application of AITC (50 μM) and Ca^{2+} (2 mM). Data were extracted from 500 ms voltage ramps (−80 to +80 mV). Scale bar, 1 s (x); y, arbitrary units. **d**, Quantification of Ca^{2+} potentiation (transient current, I_{trans}, measured 5 s after Ca^{2+} application) and desensitization (sustained current, I_{sus}, measured 60 s after Ca^{2+} application). Wild type, $n = 6$ independent experiments; E788S, $n = 8$; E788S/Q791S/N805S, $n = 10$. $^{*}P = 0.04$, $^{**}P = 0.005$, $^{****}P < 0.0001$; one-way mixed-effects analysis ANOVA with post hoc Holm–Sidak correction for multiple comparisons; Data are mean ± s.e.m. **e**, **f**, Normalized whole-cell recordings for TRPA1 channels co-expressed with M1 muscarinic acetylcholine receptor in response to bath-applied carbachol (Cbc) (100 μM; data represent $n = 7$ independent experiments for wild type and $n = 4$ for E788S mutant), with or without thapsigargin (Thg., 1 μM; $n = 5$) pre-treatment or inclusion of rapid intracellular Ca^{2+} chelators EGTA and BAPTA (1 mM each; $n = 5$). AITC, 50 μM; A-96, 10 μM. Scale bars, 1 s (x); y, arbitrary units. **g**, Quantification of responses in **e**, **f**. $^{**}P = 0.002$ for wild type versus thapsigargin (Thg.) and chelators (Chel.); $P = 0.004$ for wild type versus E788S. Kruskal–Wallis test with post hoc Dunn's correction for multiple comparisons. Data are mean ± s.e.m.

because they used relatively bulky electrophiles (benzyl isothiocyanate and JT010) that stabilize the open pocket by modifying C621 alone.

Further evidence for this model comes from measurement of channel-closure times, which reflect coupling efficiency between agonist binding and channel gating. To assess this parameter, we examined tail currents following activation of channels by membrane depolarization in the absence or presence of irreversible agonists. For wild-type TRPA1 channels, the rate of channel closure was slowed approximately threefold by IA (Extended Data Fig. 6), as expected if electrophile modification enhances coupling efficiency of A-loop reorientation to channel gating. For the C665S mutant, which retains partial sensitivity to IA, the rate of channel closure was similar to that determined without agonist (Extended Data Fig. 6a, b), suggesting that modification at C665 is important for stabilizing and coupling A-loop reorientation to gating. BODIPY–IA attaches to only one site, suggesting that bulky electrophiles stabilize active A-loop conformation by modifying C621 alone. Notably, TRPA1(C665S) showed full sensitivity to BIA with regard to response magnitude and tail-current decay time (Extended Data Fig. 6a, c), confirming this notion.

How might upward A-loop stabilization couple to channel gating? In this loop configuration, K671 is stabilized and becomes resolved through its interaction with backbone carbonyls at the C terminus of the TRP domain (Fig. 3a, b, Extended Data Fig. 7), a conserved α-helical motif that lies parallel to the inner membrane leaflet and is implicated in gating of numerous TRP channel subtypes[24]. The positively charged side chain of K671 enhances the dipole moment of the TRP helix (Extended Data Fig. 7a, b), strengthening the positive electrostatic surface potential at its N terminus (Extended Data Fig. 7c, d). We speculate that this promotes repulsion between TRP domains from neighbouring subunits, thereby biasing conformational equilibrium of the channel towards the open state by driving expansion of overlying S6 domains that constitute the lower gate (Extended Data Fig. 7e).

K671 is conserved across vertebrate TRPA1 channels (Extended Data Fig. 7f). Mutation to the cognate residue in the fly orthologue (K671A) rendered human TRPA1 insensitive to IA or to concentrations of allyl isothiocyanate (AITC) around its half-maximal effective concentration (EC_{50}) (about 30 μM), as expected if K671 is critical for propagating local conformational changes in the modified A-loop to the channel gate (Fig. 3e–g). We have previously shown that TRPA1 lacking critical cysteines retains sensitivity to high concentrations of AITC (about $10 \times EC_{50}$) and that this is mediated via modification of another lysine residue (K710) preceding the S1 transmembrane helix[3]. Indeed, we found that K671A channels are activated by 1 mM AITC, demonstrating that this mutant is functional, and that modification of K710 activates the channel through a mechanism distinct from the one we propose for cysteine modification (Fig. 3e–g). K710 is also in proximity to the TRP domain and modification at this site may induce movement in this critical helix independent of A-loop engagement.

Structurally conserved calcium control site

When TRPA1 was solubilized in LMNG, a robust density was seen at the bottom of each S2–S3 α-helix facing the cytoplasm (Fig. 4a, Extended Data Fig. 8a), where it is surrounded by residues E788, Q791, Y799, N805, and E808, typical of calcium coordination sites[25]. Indeed, this configuration is strikingly similar to a calcium-binding site seen in TRPM2, 4 and 8, with all relevant residues conserved[18,26–28] (Fig. 4a, b). Because channel purification was carried out in nominally calcium-free buffers, this density probably represents cellular calcium bound to a high-affinity site. The proximal S2–S3 loop is better resolved compared with PMAL-C8 structures, where calcium is probably lost during prolonged detergent–amphipol exchange.

Permeating calcium has two sequential effects on TRPA1: enhancing currents and then promoting desensitization[8,13]. TRPA1(E788S) lacked

calcium-mediated potentiation but retained desensitization (Fig. 4c, d), consistent with previous observations[15], whereas a triple mutant (TRPA1(E788S/Q791S/N805S)) lacked both. The ability of TRPA1 to function as a receptor-operated channel is probably mediated through consequent release of calcium from intracellular stores (although metabolism of phosphoinositide lipids has also been implicated)[12]. To investigate whether this action converges on the same calcium site identified here, we co-expressed the M1 muscarinic receptor and TRPA1 in transfected cells and recorded carbachol (an M1 agonist)-evoked TRPA1 responses in the absence of extracellular calcium. As previously shown[8], carbachol elicited robust currents that were blocked by A-96 and absent when intracellular calcium was depleted by thapsigargin pre-treatment or rapidly chelated by EGTA and BAPTA (Fig. 4e, g, Extended Data Fig. 8b, c), reaffirming calcium as the critical second messenger. Notably, the E788S mutant showed no response to carbachol (Fig. 4f, g), demonstrating that the major regulatory actions of calcium converge on this single site.

Discussion

Detectors of noxious stimuli function as early-warning systems that recognize potentially injurious events before they elicit wholesale tissue damage. To accomplish this, they must balance low threshold sensitivity with high fidelity. The two-step mechanism we propose for electrophile-mediated TRPA1 activation satisfies this requirement and may be particularly important for detecting small volatile environmental toxicants (Extended Data Fig. 9e). For larger endogenous algogens that drive inflammatory pain, signal-to-noise considerations are perhaps less relevant, since rapid recognition and escape are not critical, and thus single modification by these bulkier electrophiles may suffice (Extended Data Fig. 9f).

TRP channels contain two highly dynamic constrictions along their ion-permeation pathway (one corresponding to a canonical lower gate and another at the level of the selectivity filter) that must functionally couple to control activation by diverse stimuli. Our findings suggest that the upper restriction has evolved to serve a range of physiological functions in this ion channel superfamily: in voltage-gated potassium channels and some TRP channels (that is, TRPM2) this region is devoted largely to ion selection[27,29], whereas in TRPV1 it serves as a regulated gate[19]. In the case of TRPA1, our results suggest an intermediate function controlling dynamic ion selectivity, which probably underlies the differential ability of activators to elicit pain with or without neurogenic inflammation[23].

The calcium-binding site we identify in TRPA1 supports an emerging picture of a conserved structural motif for detecting elevated intracellular calcium over a range of concentrations resulting from channel activation and/or store release. In TRPM8 this conserved calcium-binding pocket is adjacent to a ligand-binding site, and calcium is required for channel activation by the synthetic supercooling agent, icilin[18,30,31]. Whether calcium similarly regulates TRPA1 in concert with as yet undiscovered ligands or post-translational modification[32], or how calcium binding affects gating movements remain intriguing questions for future studies.

Online content

Any methods, additional references, Nature Research reporting summaries, source data, extended data, supplementary information, acknowledgements, peer review information; details of author contributions and competing interests; and statements of data and code availability are available at https://doi.org/10.1038/s41586-020-2480-9.

1. Bautista, D. M., Pellegrino, M. & Tsunozaki, M. TRPA1: A gatekeeper for inflammation. *Annu. Rev. Physiol.* **75**, 181–200 (2013).
2. Chen, J. & Hackos, D. H. TRPA1 as a drug target—promise and challenges. *Naunyn Schmiedebergs Arch. Pharmacol.* **388**, 451–463 (2015).
3. Hinman, A., Chuang, H. H., Bautista, D. M. & Julius, D. TRP channel activation by reversible covalent modification. *Proc. Natl Acad. Sci. USA* **103**, 19564–19568 (2006).
4. Macpherson, L. J. et al. Noxious compounds activate TRPA1 ion channels through covalent modification of cysteines. *Nature* **445**, 541–545 (2007).
5. Bahia, P. K. et al. The exceptionally high reactivity of Cys 621 is critical for electrophilic activation of the sensory nerve ion channel TRPA1. *J. Gen. Physiol.* **147**, 451–465 (2016).
6. Paulsen, C. E., Armache, J. P., Gao, Y., Cheng, Y. & Julius, D. Structure of the TRPA1 ion channel suggests regulatory mechanisms. *Nature* **520**, 511–517 (2015).
7. Suo, Y. et al. Structural insights into electrophile irritant sensing by the human TRPA1 channel. *Neuron* **105**, 882–894.e5 (2020).
8. Jordt, S. E. et al. Mustard oils and cannabinoids excite sensory nerve fibres through the TRP channel ANKTM1. *Nature* **427**, 260–265 (2004).
9. Bandell, M. et al. Noxious cold ion channel TRPA1 is activated by pungent compounds and bradykinin. *Neuron* **41**, 849–857 (2004).
10. Dai, Y. et al. Sensitization of TRPA1 by PAR2 contributes to the sensation of inflammatory pain. *J. Clin. Invest.* **117**, 1979–1987 (2007).
11. Wilson, S. R. et al. The epithelial cell-derived atopic dermatitis cytokine TSLP activates neurons to induce itch. *Cell* **155**, 285–295 (2013).
12. Talavera, K. et al. Mammalian transient receptor potential TRPA1 channels: from structure to disease. *Physiol. Rev.* **100**, 725–803 (2020).
13. Wang, Y. Y., Chang, R. B., Waters, H. N., McKemy, D. D. & Liman, E. R. The nociceptor ion channel TRPA1 is potentiated and inactivated by permeating calcium ions. *J. Biol. Chem.* **283**, 32691–32703 (2008).
14. Zurborg, S., Yurgionas, B., Jira, J. A., Caspani, O. & Heppenstall, P. A. Direct activation of the ion channel TRPA1 by Ca^{2+}. *Nat. Neurosci.* **10**, 277–279 (2007).
15. Zimova, L. et al. Intracellular cavity of sensor domain controls allosteric gating of TRPA1 channel. *Sci. Signal.* **11**, eaan8621 (2018).
16. Sura, L. et al. C-terminal acidic cluster is involved in Ca^{2+}-induced regulation of human transient receptor potential ankyrin 1 channel. *J. Biol. Chem.* **287**, 18067–18077 (2012).
17. Hasan, R., Leeson-Payne, A. T. S., Jaggar, J. H. & Zhang, X. Calmodulin is responsible for Ca^{2+}-dependent regulation of TRPA1 channels. *Sci. Rep.* **7**, 45098 (2017).
18. Diver, M. M., Cheng, Y. & Julius, D. Structural insights into TRPM8 inhibition and desensitization. *Science* **365**, 1434–1440 (2019).
19. Cao, E., Liao, M., Cheng, Y. & Julius, D. TRPV1 structures in distinct conformations reveal activation mechanisms. *Nature* **504**, 113–118 (2013).
20. Karashima, Y. et al. Agonist-induced changes in Ca^{2+} permeation through the nociceptor cation channel TRPA1. *Biophys. J.* **98**, 773–783 (2010).
21. Bobkov, Y. V., Corey, E. A. & Ache, B. W. The pore properties of human nociceptor channel TRPA1 evaluated in single channel recordings. *Biochim. Biophys. Acta* **1808**, 1120–1128 (2011).
22. Christensen, A. P., Akyuz, N. & Corey, D. P. The outer pore and selectivity filter of TRPA1. *PLoS One* **11**, e0166167 (2016).
23. Lin King, J. V. et al. A cell-penetrating scorpion toxin enables mode-specific modulation of TRPA1 and pain. *Cell* **178**, 1362–1374.e16 (2019).
24. Hilton, J. K., Kim, M. & Van Horn, W. D. Structural and evolutionary insights point to allosteric regulation of TRP ion channels. *Acc. Chem. Res.* **52**, 1643–1652 (2019).
25. Wang, X., Kirberger, M., Qiu, F., Chen, G. & Yang, J. J. Towards predicting Ca^{2+}-binding sites with different coordination numbers in proteins with atomic resolution. *Proteins* **75**, 787–798 (2009).
26. Autzen, H. E. et al. Structure of the human TRPM4 ion channel in a lipid nanodisc. *Science* **359**, 228–232 (2018).
27. Huang, Y., Winkler, P. A., Sun, W., Lü, W. & Du, J. Architecture of the TRPM2 channel and its activation mechanism by ADP-ribose and calcium. *Nature* **562**, 145–149 (2018).
28. Zhang, Z., Tóth, B., Szollosi, A., Chen, J. & Csanády, L. Structure of a TRPM2 channel in complex with Ca^{2+} explains unique gating regulation. *eLife* **7**, e36409 (2018).
29. Doyle, D. A. et al. The structure of the potassium channel: molecular basis of K^+ conduction and selectivity. *Science* **280**, 69–77 (1998).
30. Chuang, H. H., Neuhausser, W. M. & Julius, D. The super-cooling agent icilin reveals a mechanism of coincidence detection by a temperature-sensitive TRP channel. *Neuron* **43**, 859–869 (2004).
31. Yin, Y. et al. Structural basis of cooling agent and lipid sensing by the cold-activated TRPM8 channel. *Science* **363**, eaav9334 (2019).
32. Meents, J. E., Fischer, M. J. M. & McNaughton, P. A. Sensitization of TRPA1 by protein kinase A. *PLoS One* **12**, e0170097 (2017).
33. Baker, N. A., Sept, D., Joseph, S., Holst, M. J. & McCammon, J. A. Electrostatics of nanosystems: application to microtubules and the ribosome. *Proc. Natl Acad. Sci. USA* **98**, 10037–10041 (2001).

Methods

No statistical methods were used to predetermine sample size. The experiments were not randomized. The investigators were not blinded to allocation during experiments and outcome assessment.

Protein expression and purification

Human TRPA1 was expressed and purified as described previously with slight modifications[6]. In brief, N-terminal-tagged MBP–TRPA1 under the control of a CMV promoter was expressed in HEK293F cells using the BacMam system (Thermo Fisher). Cells were purchased from ATCC, where they were validated and certified free of mycoplasma contamination. Protein expression was induced at an approximate cell density of 1.5×10^6 cells ml^{-1} with media supplemented with 5 mM sodium butyrate and 5 μM ruthenium red. After 16 h. at 37 °C, cells were collected by centrifugation at 1,000*g* for 10 min. Cells were resuspended in lysis buffer (50 mM HEPES, pH 8.0, 150 mM NaCl, 1 mM inositol hexakisphosphate (IP_6), 1 mM DTT, 1 mM EDTA, protease inhibitors) and lysed by sonication. Cell membranes were isolated by ultracentrifugation at ~180,000*g* for 45 min and the pellet was resuspended in lysis buffer before multiple passes through a glass homogenizer. Cell membranes were solubilized by addition of LMNG or CYMAL-5 NG (Anatrace) to a final concentration of 0.5% (w/v) and rocking at 4 °C for 1 h. Insoluble debris was removed by centrifugation at ~35,000*g* for 20 min. and the supernatant passed over amylose beads by gravity flow at 4 °C. The beads were washed with wash buffer (50 mM HEPES, pH 8.0, 150 mM NaCl, 1 mM IP_6, 1 mM DTT, 0.005% LMNG or CYMAL-5 NG) and eluted with wash buffer supplemented with 10 mM maltose.

For exchange into amphipol, PMAL-C8 was added to the detergent-solubilized sample in a 3:1 PMAL:protein ratio. The solution was mixed by rocking at 4 °C for 1 h. before addition of 100 μl bio-beads (Biorad) ml^{-1} of protein sample. The sample with bio-beads was mixed by rocking at 4 °C overnight. The bio-beads were spun down in a tabletop centrifuge at 100*g* and the supernatant analysed by size-exclusion chromatography in detergent-free buffer (50 mM HEPES, pH 8.0, 150 mM NaCl, 1 mM IP_6, 1 mM DTT). Peak fractions corresponding to TRPA1 were pooled and concentrated 0.5–2 mg ml^{-1} in a 100 kDa MWCO centrifuge concentrator.

Agonists and antagonists

To acquire samples of activated TRPA1 for structural studies, cell membranes containing TRPA1 was incubated with 100 μM IA or BODIPY–IA (Millipore Sigma) for 10 min. before protein purification. Samples of antagonist-bound TRPA1 were acquired by incubating the purified channel with 10 μM A-967079 (A-96) (Tocris) for 10 min before cryo-EM grid preparation.

Rationale and interpretation of solubilization conditions

TRPA1 protein was imaged in PMAL-C8 amphipol or LMNG detergent. When apo TRPA1 was solubilized in CYMAL-5 NG and exchanged into PMAL-C8, we observed two conformational states (closed and open) within the same sample (Fig. 1a), both of which lacked ions in the calcium binding site. However, the A-loop could not be modelled, consistent with the dynamic nature of the loop and the ability of the channel to adopt different states (Extended Data Fig. 2e). Treatment with IA stabilized the A-loop in the up conformation in conjunction with an open pore, which we therefore designated an activated state of the channel. Addition of agonist before detergent extraction from membranes was crucial for isolating the channel in the activated state, presumably because solubilization in detergent or amphipol prevents dynamic exchange between different channel conformations. Consistent with this notion, when A-96 was added after channel solubilization in PMAL-C8, the antagonist recognized, but did not shift the equilibrium towards the closed conformation. In LMNG, which produced structures of higher resolutions, the transmembrane core of the channel adopted a closed conformation under both apo and BIA conditions, possibly due to locking of the transmembrane domain by LMNG and/or desensitization of the channel by bound ions in the calcium binding site. This configuration resembles those previously described by us or Suo et al.[7]. Consistent with a strongly biased closed state, the A-loop was clearly observed in the down (closed) conformation of the apo channel. However, modification of TRPA1 by BIA stabilized the A-loop in the up (activated) conformation in conjunction with a closed pore, which likely represents an intermediate state of the channel following electrophile modification.

Cryo-EM data collection and processing

Samples for cryo-EM were prepared by applying 4 μl of purified TRPA1 to 1.2/1.3 holey carbon grids (Quantifoil) and blotting for 8–12 s. in a Vitrobot Mark IV (Thermo Fisher) before plunge freezing in liquid ethane. For multi-shot imaging, samples were prepared on 2/2 holey carbon grids (Quantifoil) and blotted for 6–8 s. Cryo-EM samples were imaged on Polara and Titan Krios microscopes (Thermo Fisher, see Extended Data Table 1 for details) equipped with the K2 Summit camera (Gatan). Movies were drift-corrected using MotionCor2[34] and CTF parameters estimated with gctf[35]. Particle images were selected from micrographs using Gautomatch (https://www.mrc-lmb.cam.ac.uk/kzhang/) and extracted in Relion[36]. Two- and three-dimensional classification of particle images was performed in cryoSPARC[37] and 3D maps refined in cryoSPARC and cisTEM[38]. Conversion of data from cryoSPARC to Relion and generation of orientation distribution plots were performed using pyem v.0.5 (https://zenodo.org/record/3576630#.XuczyFVKjIU). Directional Fourier shell correlations of cryo-EM maps were performed as previously described[39].

Model building and analysis

Cryo-EM maps were visualized with UCSF Chimera[40]. Atomic models were built into the cryo-EM maps with Coot[41] using the previously published structure of TRPA1 as a starting model (PDB ID: 3J9P). The models were refined over multiple rounds using PHENIX Real Space Refinement[42]. Ligands were built using Coot and their geometric restraints calculated with Phenix eLBOW[43]. Cysteine pK_a values were calculated in H++[44] and used to solve the Henderson–Hasselbalch equation[45,46] to determine the percentage free sulfhydryl (Extended Data Fig. 5h). Electrostatic surface potentials for the Apo-LMNG and BODIPY–IA–LMNG structures were calculated in APBS[33] using an AMBER forcefield and are displayed at ± 10 kT e^{-1} (Fig. 2d, Extended Data Figs. 3, 7).

Agonist-binding assay

Eight-hundred millilitre cultures of HEK293F cells (1.0 million cells per ml) were transfected with wild-type or mutant TRPA1 DNA using FectoPro (Polyplus Transfection) reagent. Cultures were supplemented with sodium butyrate immediately after transfection and grown for 2 days at 37 °C, 8% CO_2, and with shaking at 135 rpm. Cells were collected by centrifugation at 1,000*g* for 10 min and then resuspended in 20 ml of lysis buffer (see Methods, 'Protein expression and purification'). The cells were incubated with 100 μM BODIPY–IA (Millipore Sigma) for 10 min before TRPA1 purification (described in Methods, 'Protein expression and purification'). The fluorescence of the purified or modified protein was quantified using a plate reader (excitation/emission: 455/520 nm), normalized for protein concentration measured by TRP fluorescence (excitation/emission: 280/337 nm).

Molecular biology and cell culture

Full-length wild-type human TRPA1 in the mammalian oocyte expression vector pMO and full-length wild-type human M1 muscarinic acetylcholine receptor in the mammalian expression vector pcDNA3.1 served as templates for all physiology experiments[6,47,48]. Constructs generated from these templates were produced by Gibson assembly (New England Biolabs) and verified by sequencing. HEK293T (ATCC) cells were

cultured at 37 °C, 5% CO_2 in DMEM Complete (DMEM-C; Dulbecco's modified Eagle's medium containing 10% (v/v) heat-inactivated calf serum, 100 U ml^{-1} penicillin G and 0.1 mg ml^{-1} streptomycin). These cells were purchased from ATCC, where they were validated and certified free of mycoplasma contamination. For heterologous expression, HEK293T cells were transfected with 1 µg of TRPA1 and/or M1 with 100 ng of eGFP in pcDNA3.1, which were combined with 3× (w/w) Lipofectamine 2000 (Thermo-Fisher) for 8 h. in Opti-MEM (Thermo Fisher). Cells were then plated onto coverslips coated with 0.01% poly-L-Lysine (MW 70–150,000, MilliporeSigma) and adhered to these coverslips for at least 12 h. before use in calcium-imaging or electrophysiology experiments.

Calcium imaging

Ratiometric Ca^{2+}-imaging was carried out on transfected HEK293T cells prepared as above. Adherent cells were loaded for 30 min. in the dark at room temperature in Ca^{2+}-free Ringer's solution (140 mM NaCl, 10 mM HEPES, 5 mM KCl, 2 mM $MgCl_2$, and 10 mM glucose; pH 7.4 with NaOH; 290–300 mOsm kg^{-1}) containing 0.1 mg ml^{-1} Fura-2 AM dye and 0.02% (w/v) Pluronic F-127. Data were generated by exciting the cells with 340 then 380 nm light using a Lambda DG-4 Illuminator (Sutter), imaged with a Grasshopper3 camera (FLIR), then analysed in MetaFluor (Molecular Devices). Data were quantified as the ratio of 340 to 380 nm fluorescence after background subtraction.

Electrophysiology

Capillary pipettes from borosilicate glass with filament (outer diameter × inner diameter, 1.10 × 0.86 mm, Sutter Instruments) were fashioned and fire-polished to a resistance of 0–5 mΩ for whole-cell recordings and 5–10 mΩ for excised patch recordings. Electrophysiological data were collected at RT using an Axopatch 200B amplifier (Axon Instruments) and digitized with a Digidata 1550B (Axon Instruments). Voltage protocols were delivered and resulting currents monitored on-line with pClamp10 (Molecular Devices), then analysed off-line in pClamp or Prism (GraphPad). All electrophysiological recordings and pharmacological manipulations were carried out under laminar flow using a pressure-driven micro-perfusion system (SmartSquirt, Automate Scientific).

For whole-cell recordings, the bath solution consisted of Ca^{2+}-free Ringer's solution, and data were digitized at 10 kHz and filtered at 1 kHz. The internal solution contained 140 mM $CsMeSO_4$; 10 mM HEPES; 1 mM $MgCl_2$; and, if indicated, 1 mM each EGTA and BAPTA. The pH was set to 7.2 with CsOH and osmolarity to 300–310 mOsm kg^{-1} with sucrose. Unless otherwise stated in the figure legends, analysis of IA- and BIA-evoked TRPA1 currents in whole-cell patch-clamp mode was carried out at V_{hold} = −80 mV. Current–voltage relationships were then measured at steady state in response to voltage steps (500 ms) from −80 to 80 mV in 10 mV increments using online leak subtraction (*P*/4). Tail currents were then evoked by a 250 ms test pulse of −120 mV. The decay-time constant τ for each tail current was determined by fitting a one-phase exponential decay function in pClamp to the tail-current obtained following the 80 mV step[49]. For analysis of Ca^{2+}-modulation, TRPA1 currents were continuously monitored over a 500 ms voltage ramp from −80 to 80 mV. Inside-out excised-patch recordings were carried out in symmetrical solutions of 150 mM NaCl, 10 mM HEPES, 2 mM EGTA, 1 mM $MgCl_2$, and 1 mM IP_6; pH 7.3 with NaOH; 300–310 mOsm kg^{-1} at a constant holding voltage of −40 mV; sampled at 20 kHz; and filtered at 2 kHz.

Statistics and experimental design

Electrophysiological data are presented as mean ± s.e.m. unless otherwise noted. We carried out statistical testing in Prism (GraphPad). Where appropriate, we used parametric significance tests assuming equal variance and a normal distribution of data. Where either of these assumptions were violated, we used non-parametric tests, as indicated in the figure legends. Choice of tests were justified given the experimental design; they are standard tests for similar experiments. For all tests, a priori, we set $\alpha = 0.05$ and represent statistical significance with the *P* value, as indicated in the figure legends. We selected sample sizes for all experiments based on our laboratory and others' experience with similar assays, and in consideration of reagent availability and technical feasibility. We made no predetermination of sample size and thus carried out the minimum number of biological replicates required for strong inference and reproducibility, as indicated in the figure legends.

Reporting summary

Further information on research design is available in the Nature Research Reporting Summary linked to this paper.

Data availability

Cryo-EM maps have been deposited in the Electron Microscopy Data Bank under accession codes EMD-21127, EMD-21128, EMD-21129, EMD-21130, EMD-21131, EMD-21537 and EMD-21538. Atomic models have been deposited in the Protein Data Bank under accession numbers 6V9V, 6V9W, 6V9X and 6V9Y.

34. Zheng, S. Q. et al. MotionCor2: anisotropic correction of beam-induced motion for improved cryo-electron microscopy. *Nat. Methods* **14**, 331–332 (2017).
35. Zhang, K. Gctf: real-time CTF determination and correction. *J. Struct. Biol.* **193**, 1–12 (2016).
36. Zivanov, J. et al. New tools for automated high-resolution cryo-EM structure determination in RELION-3. *eLife* **7**, e42166 (2018).
37. Punjani, A., Rubinstein, J. L., Fleet, D. J. & Brubaker, M. A. cryoSPARC: algorithms for rapid unsupervised cryo-EM structure determination. *Nat. Methods* **14**, 290–296 (2017).
38. Grant, T., Rohou, A. & Grigorieff, N. cisTEM, user-friendly software for single-particle image processing. *eLife* **7**, e35383 (2018).
39. Dang, S. et al. Cryo-EM structures of the TMEM16A calcium-activated chloride channel. *Nature* **552**, 426–429 (2017).
40. Pettersen, E. F. et al. UCSF Chimera—a visualization system for exploratory research and analysis. *J. Comput. Chem.* **25**, 1605–1612 (2004).
41. Emsley, P., Lohkamp, B., Scott, W. G. & Cowtan, K. Features and development of Coot. *Acta Crystallogr. D* **66**, 486–501 (2010).
42. Afonine, P. V. et al. Real-space refinement in PHENIX for cryo-EM and crystallography. *Acta Crystallogr. D* **74**, 531–544 (2018).
43. Moriarty, N. W., Grosse-Kunstleve, R. W. & Adams, P. D. Electronic Ligand Builder and Optimization Workbench (eLBOW): a tool for ligand coordinate and restraint generation. *Acta Crystallogr. D* **65**, 1074–1080 (2009).
44. Anandakrishnan, R., Aguilar, B. & Onufriev, A. V. H. H++ 3.0: automating pK prediction and the preparation of biomolecular structures for atomistic molecular modeling and simulations. *Nucleic Acids Res.* **40**, W537–W541 (2012).
45. Henderson, L. J. Concerning the relationship between the strength of acids and their capacity to preserve neutrality. *Am. J. Physiol.* **21**, 173–179 (1908).
46. Hasselbalch, K. A. Die Berechnung der Wasserstoffzahl des Blutes aus der freien und gebundenen Kohlensäure desselben, und die Sauerstoffbindung des Blutes als Funktion der Wasserstoffzahl. *Biochem. Z.* **78**, 112–114 (1917).
47. Cordero-Morales, J. F., Gracheva, E. O. & Julius, D. Cytoplasmic ankyrin repeats of transient receptor potential A1 (TRPA1) dictate sensitivity to thermal and chemical stimuli. *Proc. Natl Acad. Sci. USA* **108**, E1184–E1191 (2011).
48. Gracheva, E. O. et al. Molecular basis of infrared detection by snakes. *Nature* **464**, 1006–1011 (2010).
49. Sakmann, B. & Neher, E. (eds) *Single-Channel Recording* (Springer, 2009).

Acknowledgements Some data for this study were collected at the Toronto High-Resolution High-Throughput cryo-EM facility, supported by the Canada Foundation for Innovation and Ontario Research Fund. This work was supported by an American Heart Association Postdoctoral Fellowship (J.Z.), a Banting Postdoctoral Fellowship from the Canadian Institutes of Health Research (J.Z.), an NSF Graduate Research Fellowship (No. 1650113 to J.V.L.K.), a UCSF Chuan-Lyu Discovery Fellowship (J.V.L.K.), a Helen Hay Whitney Foundation Postdoctoral Fellowship (C.E.P.) and grants from the NIH (R35 NS105038 to D.J; R01 GM098672, S10 OD021741, and S10 OD020054 to Y.C.; T32 HL007731 to C.E.P.; and T32 GM007449 to J.V.L.K.). Y.C. is an Investigator of the Howard Hughes Medical Institute.

Author contributions J.Z. designed and executed biochemical and cryo-EM experiments, with early collaborative contribution and guidance on TRPA1 expression and purification from C.E.P. J.V.L.K. designed and carried out physiology experiments. J.Z., J.V.L.K, Y.C. and D.J. conceived the project, interpreted the results, and wrote the manuscript.

Competing interests The authors declare no competing interests.

Additional information
Supplementary information is available for this paper at https://doi.org/10.1038/s41586-020-2480-9.

Correspondence and requests for materials should be addressed to Y.C. or D.J.

Peer review information *Nature* thanks Thomas Taylor-Clark and the other, anonymous, reviewer(s) for their contribution to the peer review of this work.

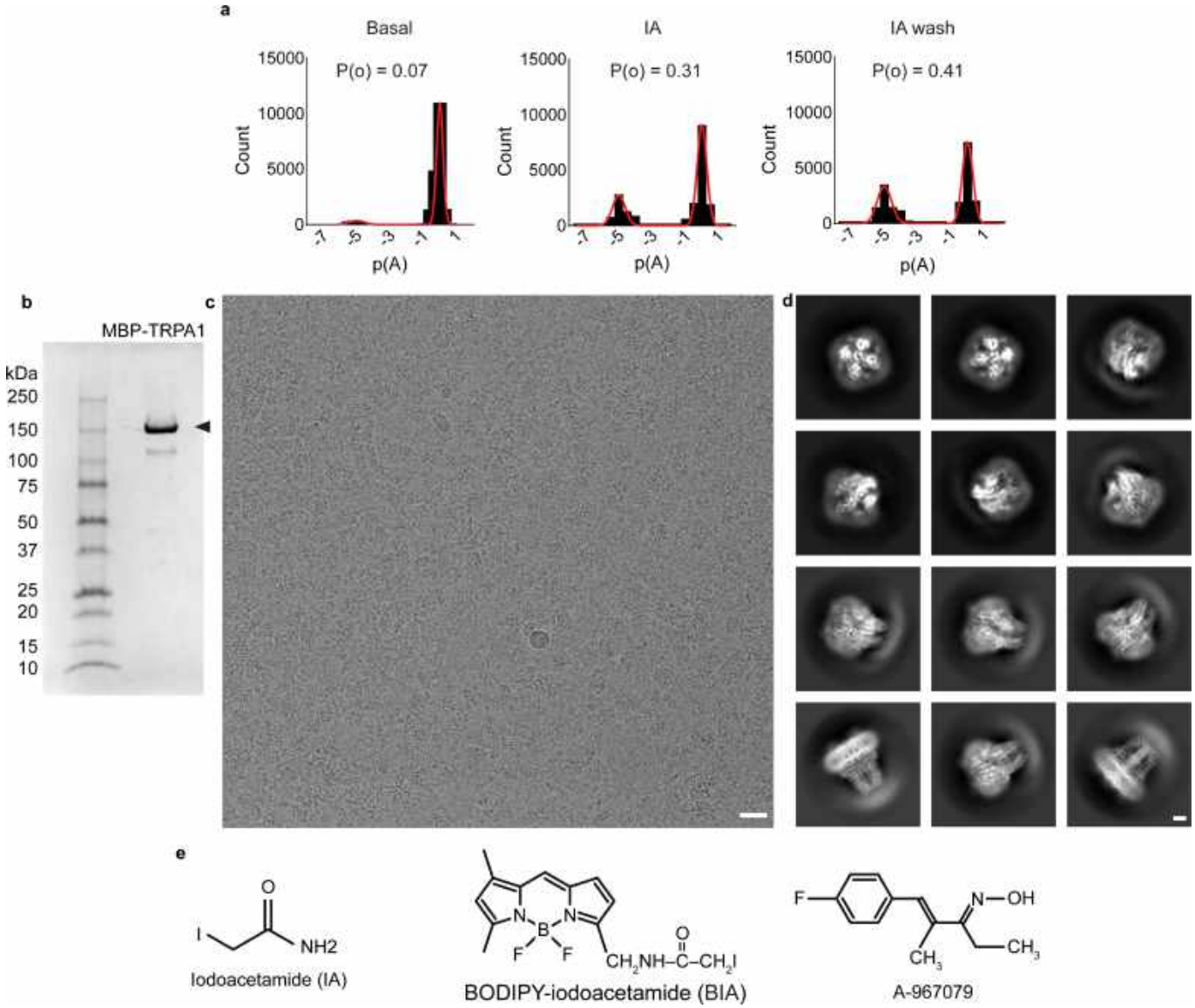

Extended Data Fig. 1 | Pharmacology and cryo-EM data collection and processing for TRPA1. a, All points histograms depicting the change in open probability (P(o)) in a single TRPA1 channel in response to IA application. Data represent $n = 9$ independent excised inside-out patches. $V_{hold} = -40$ mV. **b**, SDS–PAGE showing MBP–TRPA1 (arrowhead) after pull-down and elution from amylose beads. **c**, Cryo-EM image of MBP–TRPA1. Scale bar, 20 nm. **d**, Two-dimensional classification of cryo-EM particle images showing TRPA1 in different orientations. Scale bar, 25 Å. **e**, Pharmacological agents used in this study.

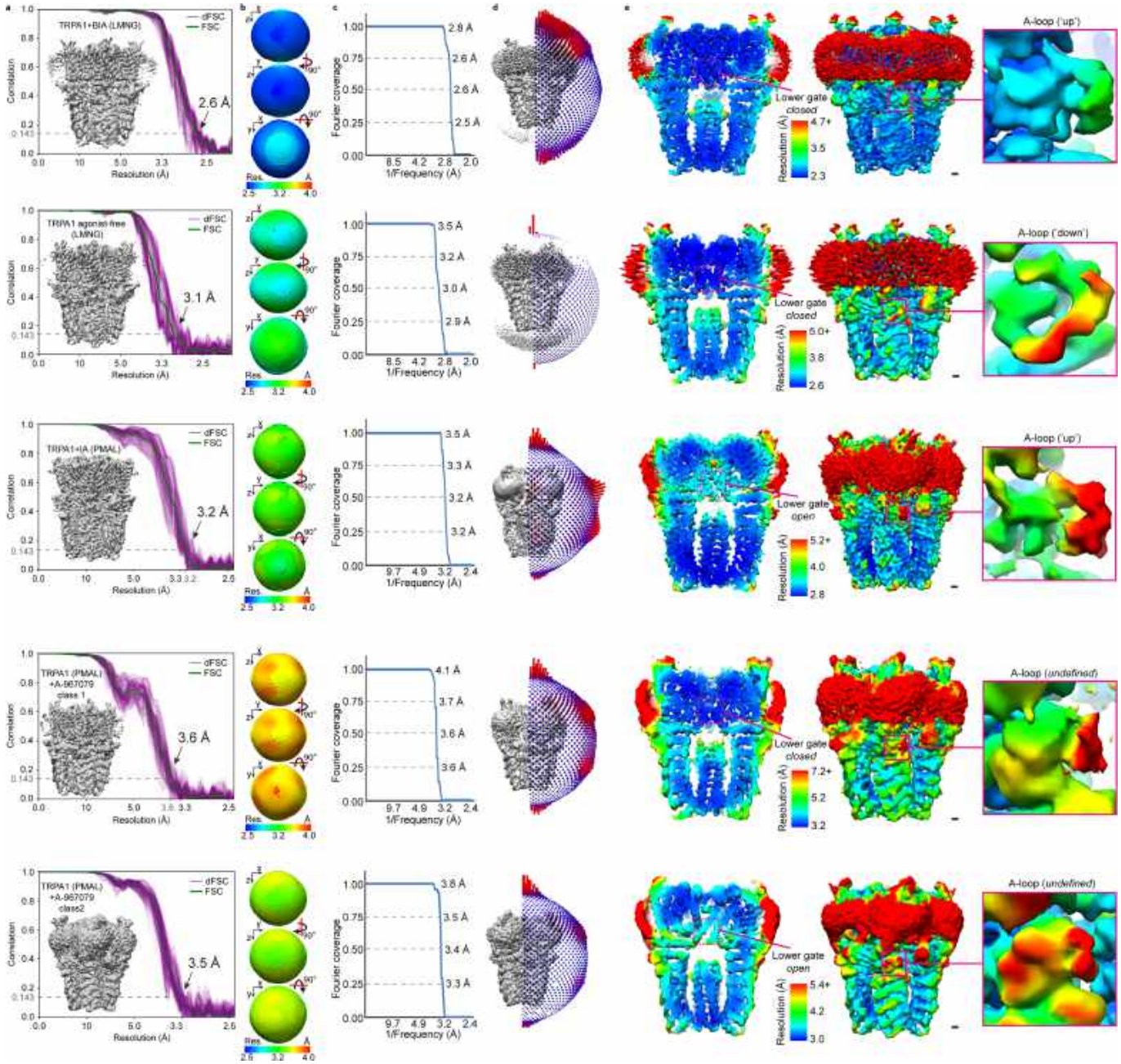

Extended Data Fig. 2 | Fourier shell correlation of cryo-EM maps, orientation distribution of particle image views, and local resolution of TRPA1 cryo-EM maps. a, Fourier shell correlation and 1D directional Fourier shell correlation plots. TRPA1 (PMAL) + A-96 class 2 denotes the structure derived from 3D classification of antagonist-treated samples in PMAL and repre\sents the open state channel without antagonist bound. **b**, Three-dimensional representations of the directional Fourier shell correlation. **c**, Fourier space covered, based on dFSC at 0.143. **d**, Orientation distribution of particle image refinement angles. **e**, The A-loop is lower resolution than surrounding map regions, indicating its dynamic nature. In the activated (TRPA1 + iodoacetamide) and open (TRPA1 + A967079 PMAL-C8 class 2) state conformations, the bottom of S6 is lower resolution than surrounding regions, indicating structural flexibility at the level of the lower gate. Scale bars, 5 Å.

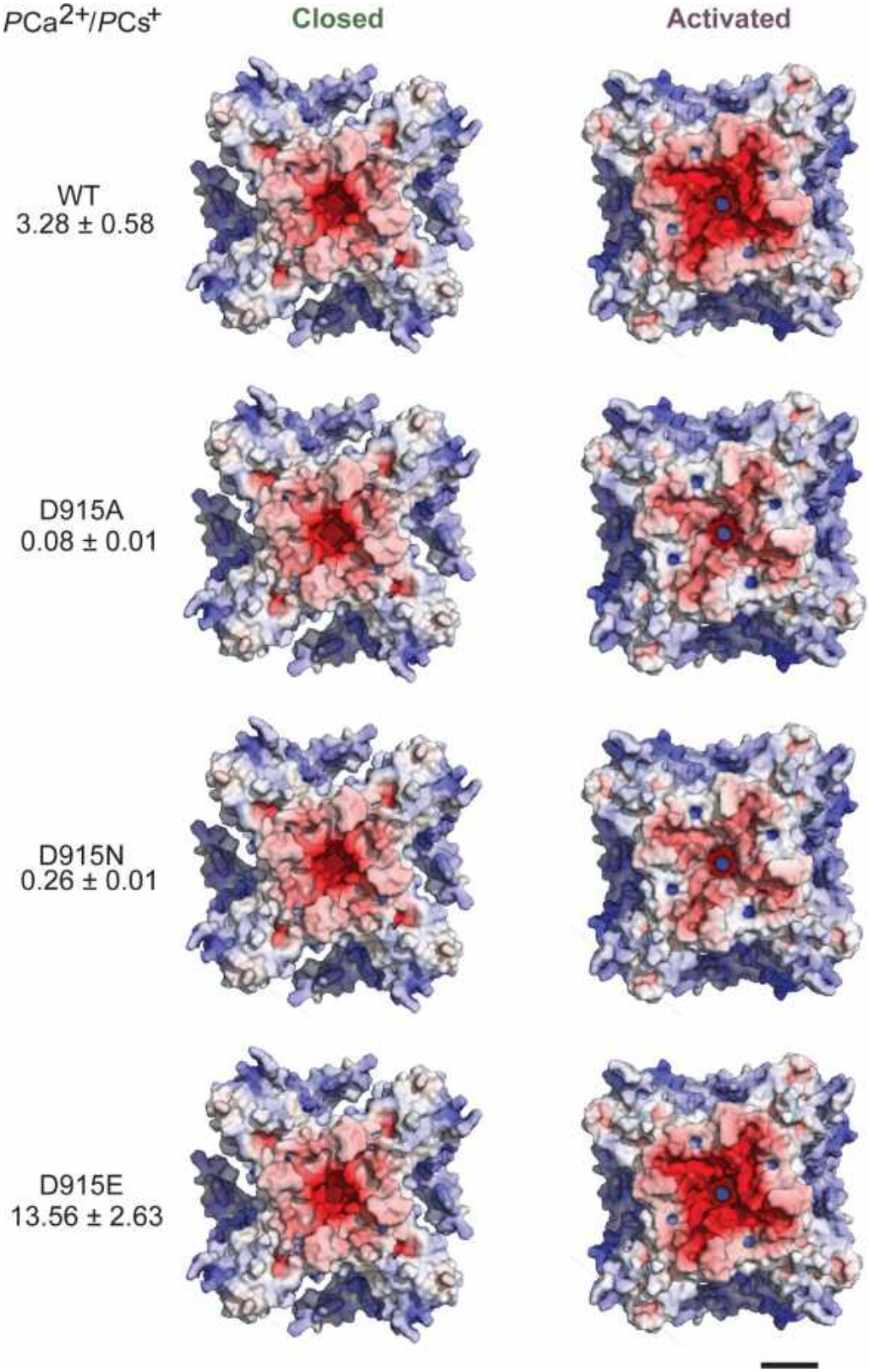

Extended Data Fig. 3 | Surface charge distribution of TRPA1's extracellular face. Electrostatic potential maps were calculated in APBS and are displayed at ±10 kT e^{-1}. In silico mutations of D915 were modelled and experimentally determined relative permeability ratios for these mutations sourced from ref. [13]. Scale bar, 30 Å.

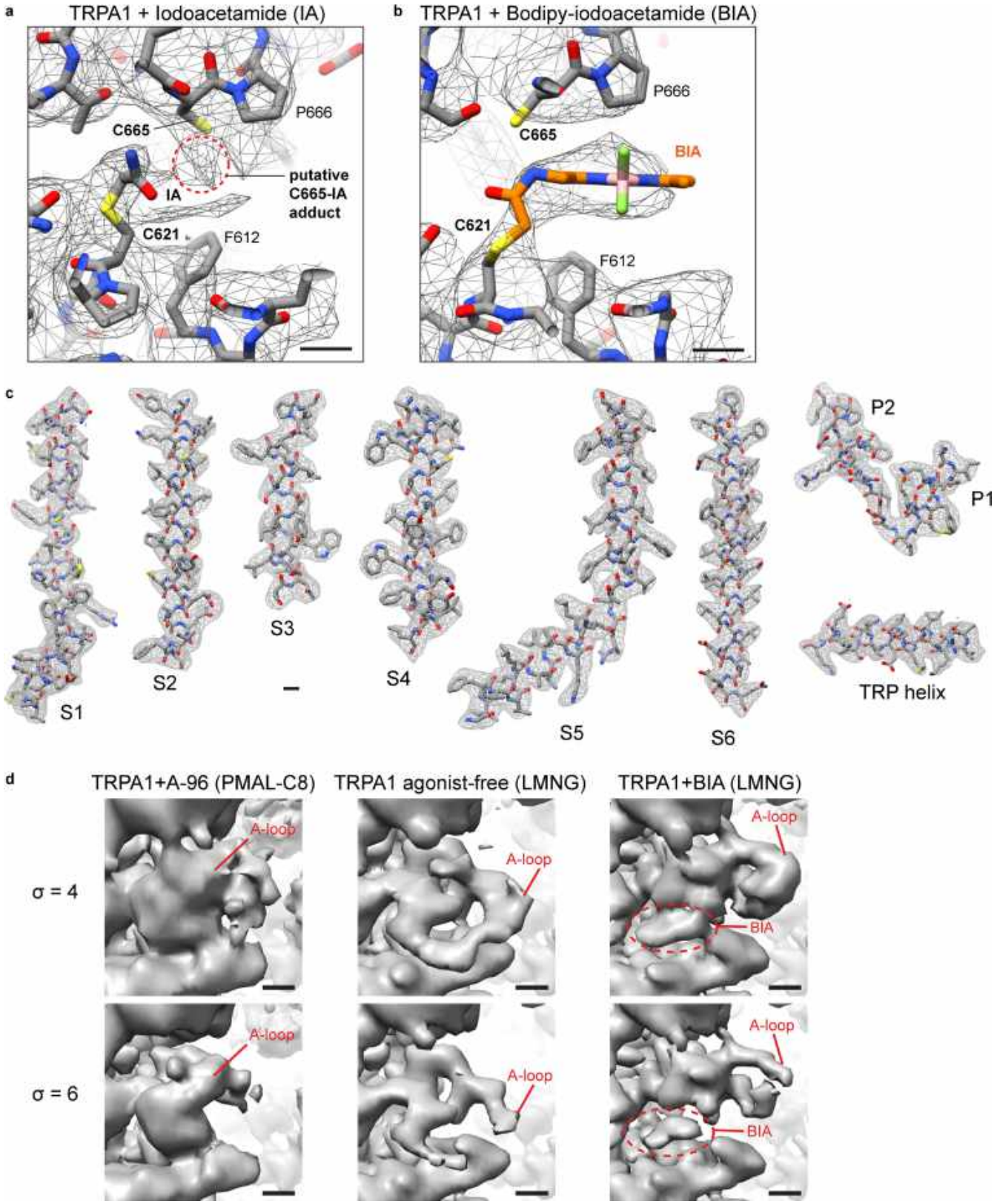

Extended Data Fig. 4 | Map densities of agonists and transmembrane α-helices. a, Strong density is observed for iodoacetamide bound to C621. Weaker density is observed next to C665, which indicate that some of the channels may be modified by agonist at this site. Map threshold: $\sigma = 4$. **b**, Clear density for BIA is observed bound to C621. No additional density is observed next to C665 in this case. Map threshold: $\sigma = 6$. **c**, Segmented map densities and atomic models for TRPA1 + BIA (LMNG). Scale bars, 3 Å. **d**, Map density of the A-loop in different states: undefined (TRPA1 + A-96, PMAL-C8), down (TRPA1 agonist-free, LMNG), and up (TRPA1 + BIA, LMNG). Densities are shown at two different thresholds ($\sigma = 4$ and 6). Scale bars, 5 Å.

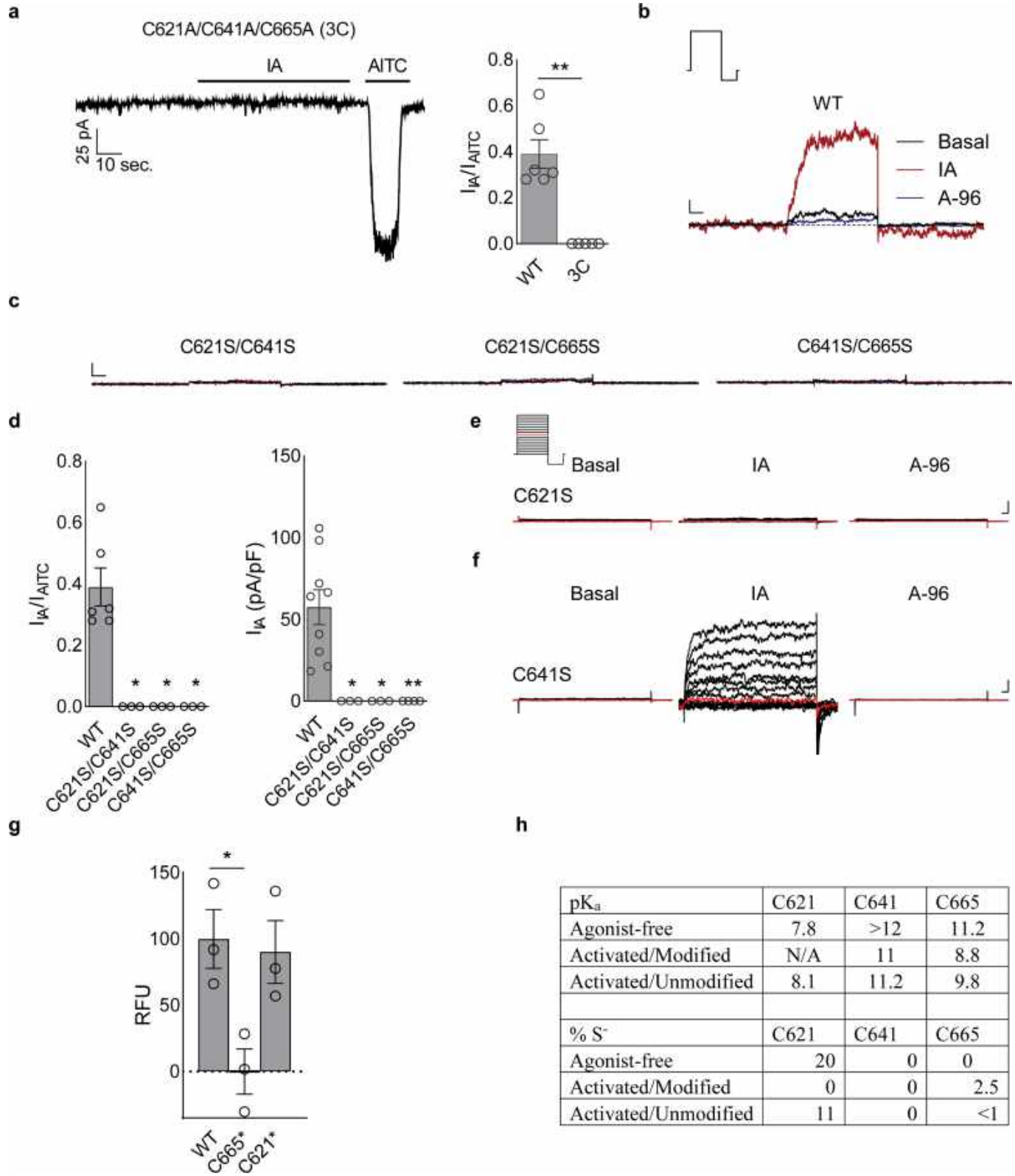

pK_a	C621	C641	C665
Agonist-free	7.8	>12	11.2
Activated/Modified	N/A	11	8.8
Activated/Unmodified	8.1	11.2	9.8
% S^-	C621	C641	C665
Agonist-free	20	0	0
Activated/Modified	0	0	2.5
Activated/Unmodified	11	0	<1

Extended Data Fig. 5 | See next page for caption.

Extended Data Fig. 5 | Characterization of TRPA1 activation by IA and BIA. **a**, IA (100 μM) activates TRPA1 through covalent modification of cysteines; AITC (250 or 1,000 μM). Data represent $n = 6$ (WT) or 5 (3C) independent experiments. $^{**}P = 0.002$, two-tailed Mann–Whitney test; $V_{hold} = -80$ mV. **b**, **c**, No single cysteine is sufficient for TRPA1 activation by IA. WT, data represent $n = 9$ independent experiments; C621S/C641S $n = 3$; C621S/C665S, $n = 3$; and C641S/C665S, $n = 4$. Data were acquired in whole-cell patch-clamp mode and reflect the results of 500-ms test pulse (80 mV). $V_{hold} = -80$ mV. Doses: IA, 100 μM; A-96, 10 μM; AITC, 250 or 1,000 μM. Scale bars, *x*, 50 ms; *y*, 100 pA. $I = 0$, dashed line. **d**, Quantification of double cysteine mutant data. Left, WT, $n = 6$ independent experiments; C621S/C641S $n = 3$; C621S/C665S, $n = 3$; and C641S/C665S, $n = 3$. $V_{hold} = -80$ mV. Right, WT, data represent $n = 9$ independent experiments; C621S/C641S $n = 3$; C621S/C665S, $n = 3$; and C641S/C665S, $n = 4$. Doses: IA, 100 μM; A-96, 10 μM; AITC, 250 or 1,000 μM. $^{*}P = 0.02$; $^{**}P = 0.007$, Kruskal–Wallis test with post hoc Dunn's test to correct for multiple comparisons. **e**, **f**, C621S displays complete loss of IA sensitivity while C641S retains full sensitivity. Data represent $n = 5$ independent experiments/construct. Data were acquired in whole-cell patch-clamp mode and reflect the results of 500-ms test pulses from −80 to 80 mV. $V_{hold} = -80$ mV. Doses: IA, 100 μM; A-96, 10 μM. Scale bars, *x*, 25 ms; *y*, 100 pA. **g**, Binding of BIA to TRPA1 C641S/C665S double mutant (C621*) is similar to wild type. Statistical significance is represented as the results of one-way ANOVA with post hoc Holm–Sidak correction for multiple comparisons; $^{*}P = 0.03$; $n = 3$ independent experiments per construct. **h**, TRPA1 cysteine pK_a values and deduced proportion of thiolate in the agonist-free state (PDB ID: 6V9W), and IA-bound ('activated', PDB ID: 6V9V) state in the presence or absence of covalent modification at C621. Data are mean ± s.e.m.

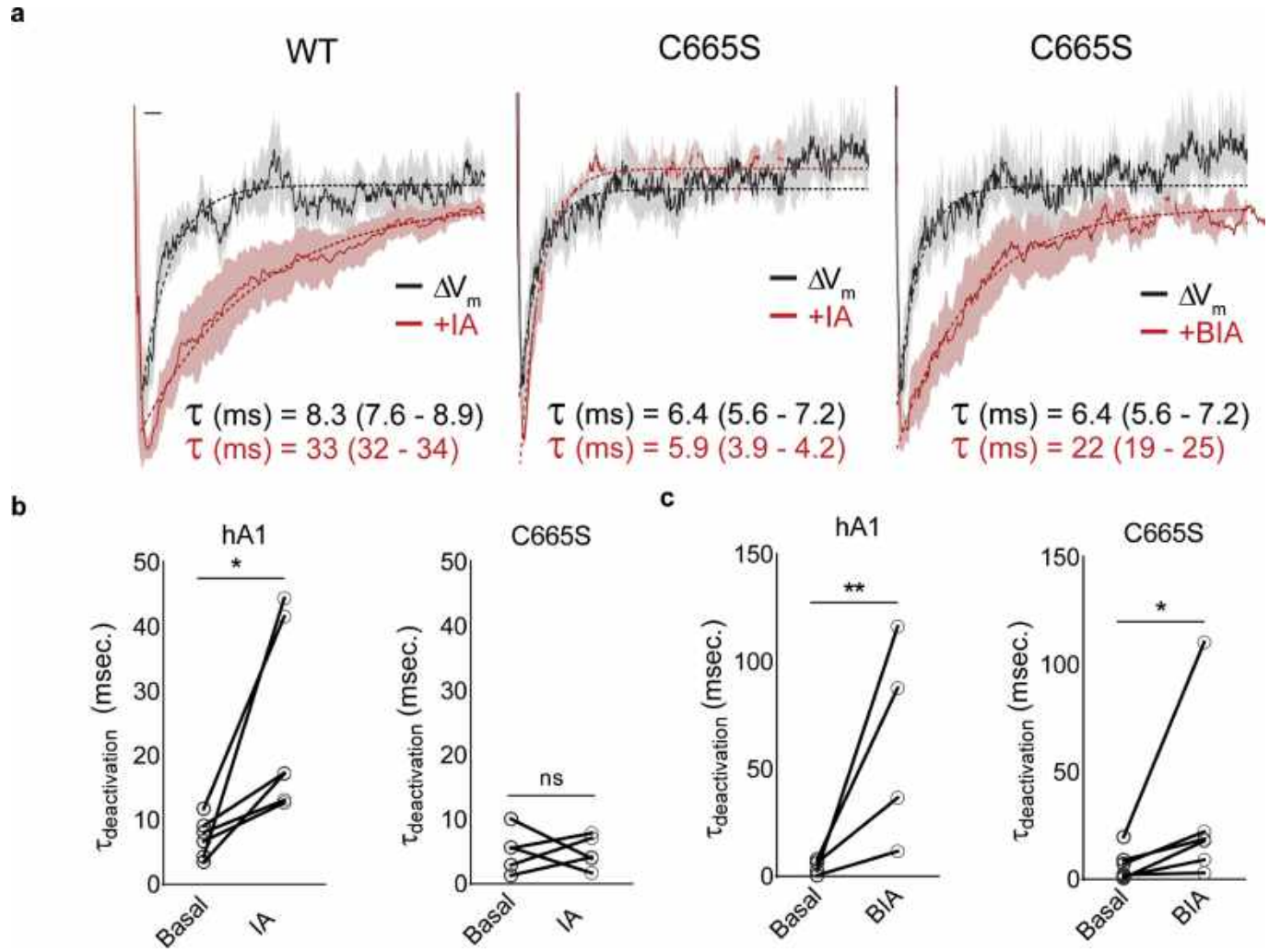

Extended Data Fig. 6 | Analysis of TRPA1 tail currents. a, Scaled averaged basal (WT, $n = 10$ independent experiments; C665S, $n = 6$), IA (100 μM; WT, $n = 5$; C665S, $n = 5$), or BIA (100 μM; C665S, $n = 6$)-evoked tail currents for TRPA1 WT and C665S mutant channels. Mean deactivation time constants (τ) are shown with 95% CI in parentheses. Scale bar, *x*, 5 ms; *y*, arbitrary units. Data were acquired in whole-cell patch-clamp mode after a 500-ms pre-pulses (−80 to 80 mV in 10 mV increments) followed by a 250-ms test pulse (−120 mV). $V_{hold} = -80$ mV. **b**, **c**, Quantification of changes in IA (**b**) and BIA (**c**) -evoked TRPA1 tail-current decay time constants in WT and C665S TRPA1. Statistical significance is represented as the results of a ratio paired two-tailed Student's *t*-test; in **b**, $^{*}P = 0.01$; in **c**, $^{*}P = 0.02$, $^{**}P = 0.009$.

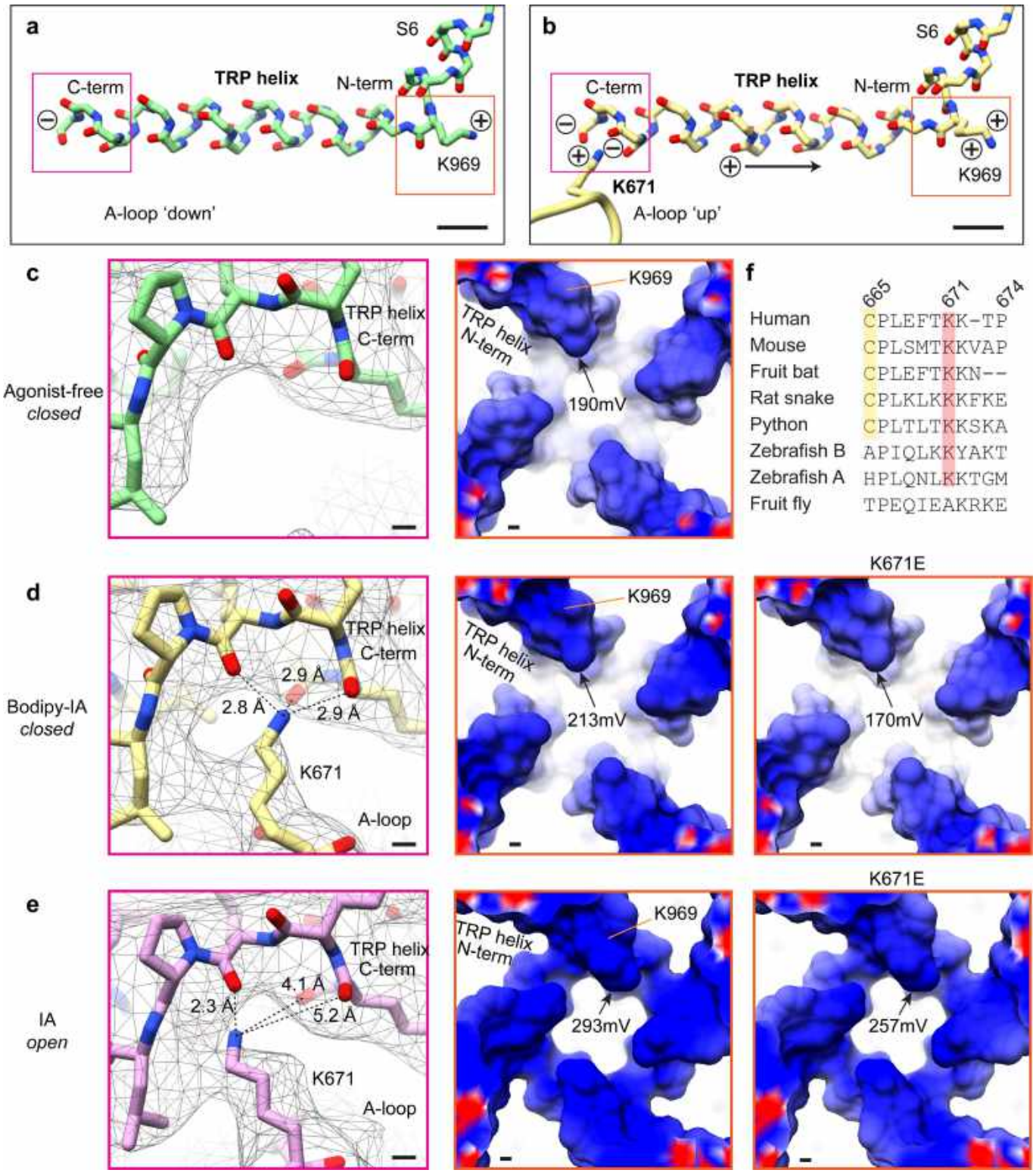

Extended Data Fig. 7 | Positive electrostatic potential below the lower gate. **a**, The TRP helix forms an electric dipole with electro-positive K969 at the N terminus and electronegative carbonyl oxygens at the C terminus. **b**, When the A-loop is oriented in the up position, K671 is coordinated by the carbonyl oxygens at the C terminus of the TRP helix and increases its dipole moment to enhance the positive electrostatic potential at the N terminus. **c**, The C-terminal carbonyl oxygens of the TRP helix form a pocket that is unoccupied in the agonist-free channel. **d**, Coordination of K671 with the carbonyl oxygens at the TRP helix C terminus increases the positive electrostatic potential at the TRP helix N terminus. In silico substitution of K671 with glutamate decreases the electrostatic potential of the TRP helix. **e**, Conformational changes associated with pore dilation further increase the positive electrostatic potential of the TRP domain. **f**, Multiple sequence alignment of TRPA1 orthologues.

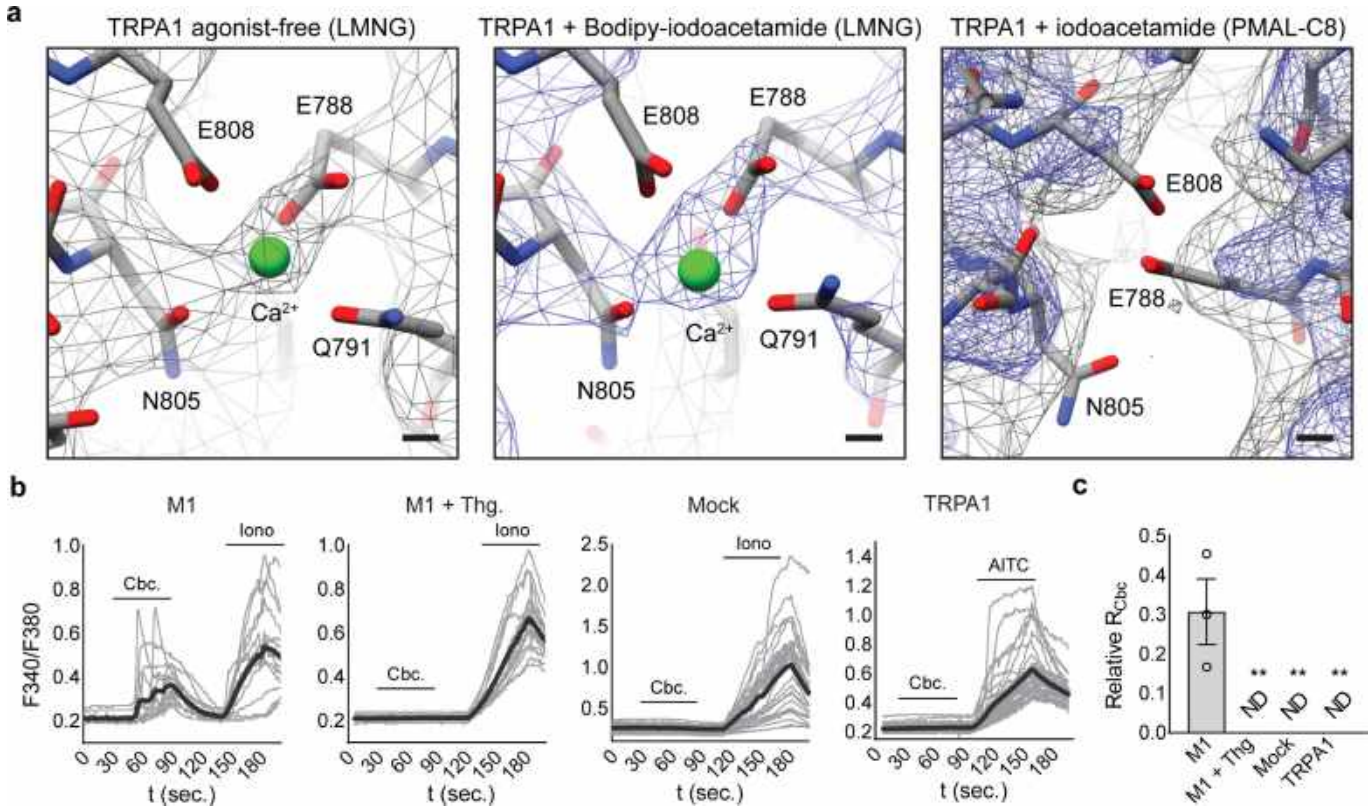

Extended Data Fig. 8 | Calcium map densities and calcium-imaging of Ca^{2+} modulation. a, Calcium is bound in both agonist-free ($\sigma = 4$) and agonist-treated ($\sigma = 8$) samples in LMNG detergent, with E788 and N805 displaying the most robust densities coordinating calcium. No density for calcium is observed for the channel in amphipol (grey, $\sigma = 4$; blue, $\sigma = 8$). **b**, Carbachol (Cbc., 100 µM) evokes intracellular Ca^{2+}-release through activation of the M1 muscarinic acetylcholine receptor. Cbc. was applied in Ca^{2+}-free Ringer's solution with 1 mM EGTA to isolate intracellular responses. $n = 16$ (M1), 18 (M1 + Thg.), 33 (Mock), or 44 (TRPA1) cells. Each graph represent $n = 3$ (M1, M1 + Thg.), 4 (Mock), or 5 (TRPA1) independent experiments. Iono., ionomycin 1 µM; thapsigargin, 1 µM; AITC, 50 µM. Grey traces represent individual cells and black traces the average of all cells in a given experiment. **c**, Quantification of Ca^{2+}-imaging experiments. The ratio evoked by Cbc. was normalized to the ionomycin-evoked response, or in TRPA1-transfected cells, the AITC-evoked response. *$P < 0.01$, Kruskal–Wallis test with post hoc Dunn's test to correct for multiple comparisons; $n = 3$ (M1, M1 + Thg.), 4 (Mock), or 5 (TRPA1) independent experiments. ND, response not detected. Data are mean ± s.e.m.

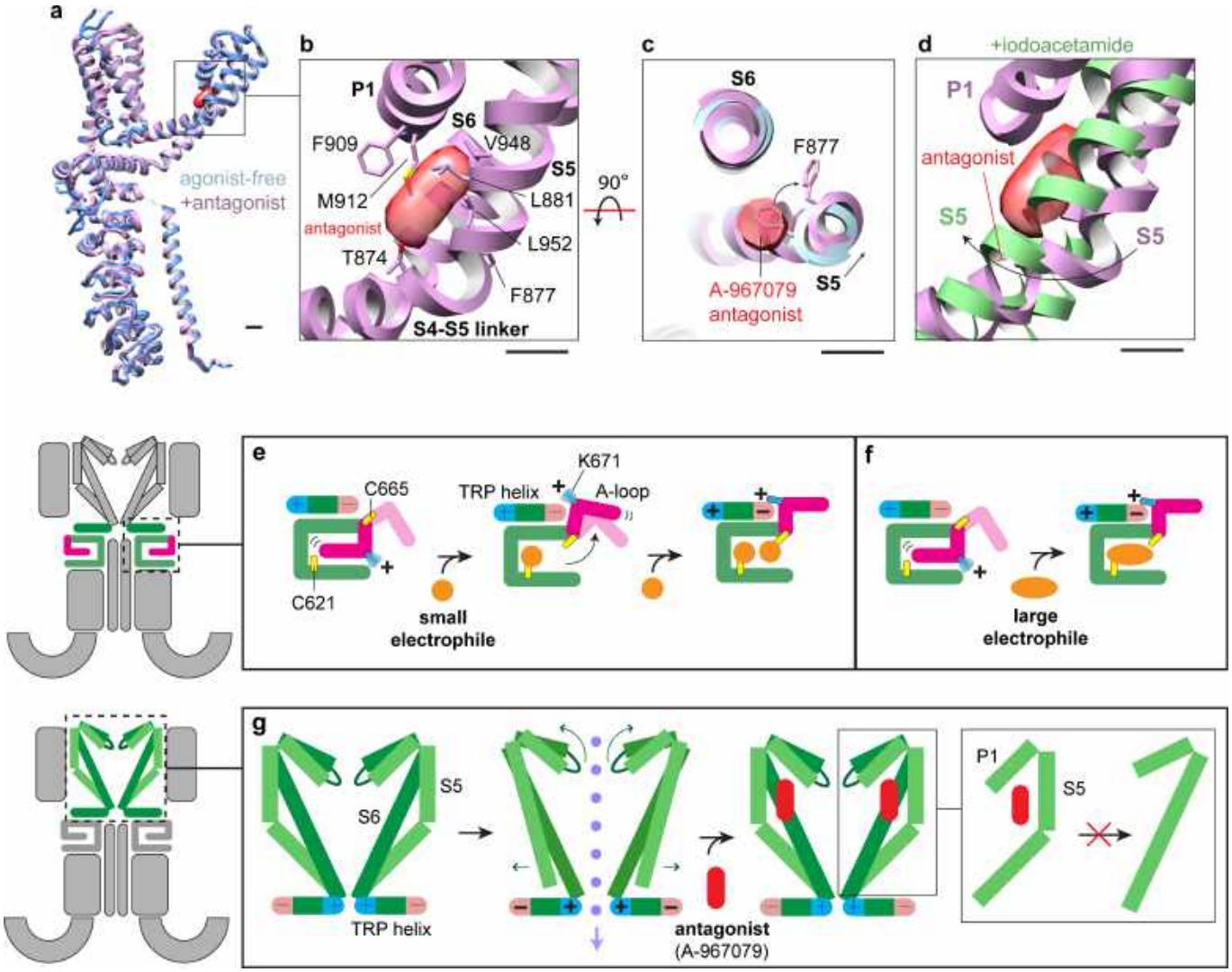

Extended Data Fig. 9 | Binding of A-96 to TRPA1 and 2-step model of electrophile action. a, The overall architecture of agonist-free and antagonist-bound TRPA1 is similar, representing a closed state. **b**, A-96 binds at the elbow of S5, sandwiched between S6 and P1. **c**, Binding of A-96 results in a slight shift in S5 and repositioning of F877. **d**, The antagonist is in an ideal position to block the straightening of the S5 elbow and inhibit channel gating. **e**, Two-step model of electrophile action on TRPA1. Attachment of a small electrophile to C621 results in A-loop rearrangement to the up position, bringing C665 into the reactive pocket. Modification of C665 by a second small electrophile stabilizes the A-loop in the up conformation and positions K671 at the C terminus of the TRP helix, enhancing the electric dipole of this region. **f**, Attachment of a large electrophile to C621 is sufficient to stabilize the A-loop in the up conformation and activate the channel. **g**, Increased positive electrostatic potential and charge repulsion at N termini of adjacent TRP helices initiates conformational changes associated with dilation of the lower gate. These movements are coupled to widening of the upper gate and selectivity filter through straightening of the S5 helix. The antagonist A-96 binds to the bent elbow region of S5, inhibiting straightening of the α-helix required for channel gating.

Extended Data Table 1 | Cryo-EM data collection, refinement and validation statistics

	TRPA1+BIA (LMNG) (EMD-21127) (PDB 6V9V)	TRPA1 agonist-free (LMNG) (EMD-21128) (PDB 6V9W)	TRPA1+IA (PMAL-C8) (EMD-21129) (PDB 6V9X)	TRPA1+A-96 (PMAL-C8) Class 1 (EMD-21130) (PDB 6V9Y)	TRPA1+A-96 (PMAL-C8) Class 2 (EMD-21131)
Data collection and processing					
Magnification	22,500	75,000	31,000	31,000	31,000
Voltage (kV)	300	300	300	300	300
Electron exposure (e–/Å^2)	25	30	40	40	40
Defocus range (μm)	0.8-2.0	0.8-2.0	1.3-2.5	1.3-2.5	1.3-2.5
Pixel size (Å)	1.05	1.06	1.22	1.22	1.22
Symmetry imposed	C4	C4	C4	C4	C4
Initial particle images (no.)	374,863	242,399	456,208	296,991	296,991
Final particle images (no.)	212,751	130,595	190,112	30,321	78,959
Map resolution (Å)	2.6	3.1	3.3	3.6	3.5
FSC threshold	0.143	0.143	0.143	0.143	0.143
Map resolution range (Å)	2.3-4.1	2.6-5.2	2.8-5.6	3.2-8.5	3.1-6.5
Refinement					
Initial model used (PDB code)	3J9P	3J9P	3J9P	3J9P	
Model resolution (Å)	2.8	3.4	3.4	3.8	
FSC threshold	0.5	0.5	0.5	0.5	
Model resolution range (Å)	357-2.8	360-3.4	311-3.4	311-3.8	
Map sharpening *B* factor (Å^2)	-25	-25	-100	-100	
Model composition					
Non-hydrogen atoms	18,976	18,812	18,084	17,716	
Protein residues	2,384	2,388	2,280	2,248	
Ligands	8	4	4	0	
B factors (Å^2)					
Protein	89	165	55	112	
Ligand	112	216	57	0	
R.m.s. deviations					
Bond lengths (Å)	0.008	0.008	0.004	0.009	
Bond angles (°)	0.904	0.965	0.880	1.179	
Validation					
MolProbity score	1.57	1.62	1.48	1.99	
Clashscore	3.47	4.53	3.52	6.53	
Poor rotamers (%)	1.2	1.21	1.24	2.13	
Ramachandran plot					
Favored (%)	94.6	95.26	96.07	94.38	
Allowed (%)	5.4	4.74	3.93	5.62	
Disallowed (%)	0.0	0.0	0.0	0.0	

	TRPA1 class 1 (PMAL-C8) (EMD-21537)	TRPA1 class 2 (PMAL-C8) (EMD-21538)
Data collection and processing		
Magnification	31,000	31,000
Voltage (kV)	300	300
Electron exposure (e–/Å^2)	40	40
Defocus range (μm)	0.5-4.5	0.5-4.5
Pixel size (Å)	1.22	1.22
Symmetry imposed	C4	C4
Initial particle images (no.)	53,301	53,301
Final particle images (no.)	15,557	28,558
Map resolution (Å)	5.9	4.3
FSC threshold	0.143	0.143
Map resolution range (Å)	4.8-8.7	3.8-6.7

Corresponding author(s): Yifan Cheng, yifan.cheng@ucsf.edu
David Julius, david.julius@ucsf.edu

Last updated by author(s): Apr 13, 2020

Reporting Summary

Nature Research wishes to improve the reproducibility of the work that we publish. This form provides structure for consistency and transparency in reporting. For further information on Nature Research policies, see Authors & Referees and the Editorial Policy Checklist.

Statistics

For all statistical analyses, confirm that the following items are present in the figure legend, table legend, main text, or Methods section.

n/a	Confirmed	
☐	☒	The exact sample size (*n*) for each experimental group/condition, given as a discrete number and unit of measurement
☐	☒	A statement on whether measurements were taken from distinct samples or whether the same sample was measured repeatedly
☐	☒	The statistical test(s) used AND whether they are one- or two-sided *Only common tests should be described solely by name; describe more complex techniques in the Methods section.*
☐	☒	A description of all covariates tested
☐	☒	A description of any assumptions or corrections, such as tests of normality and adjustment for multiple comparisons
☐	☒	A full description of the statistical parameters including central tendency (e.g. means) or other basic estimates (e.g. regression coefficient) AND variation (e.g. standard deviation) or associated estimates of uncertainty (e.g. confidence intervals)
☐	☒	For null hypothesis testing, the test statistic (e.g. *F*, *t*, *r*) with confidence intervals, effect sizes, degrees of freedom and *P* value noted *Give P values as exact values whenever suitable.*
☒	☐	For Bayesian analysis, information on the choice of priors and Markov chain Monte Carlo settings
☒	☐	For hierarchical and complex designs, identification of the appropriate level for tests and full reporting of outcomes
☒	☐	Estimates of effect sizes (e.g. Cohen's *d*, Pearson's *r*), indicating how they were calculated

Our web collection on statistics for biologists contains articles on many of the points above.

Software and code

Policy information about availability of computer code

Data collection	Commercial software or open-source software was used in all cases; specifically, pClamp and MetaFluor
Data analysis	Commercial software or open-source software was used in all cases; including: pClamp, MetaFluor, UCSF Chimaera, PyMol, Graphpad Prism, JalView, MotionCor2, gctf, gautomatch, Relion, cryoSPARC, cisTEM, PHENIX, COOT, and pyem.

For manuscripts utilizing custom algorithms or software that are central to the research but not yet described in published literature, software must be made available to editors/reviewers. We strongly encourage code deposition in a community repository (e.g. GitHub). See the Nature Research guidelines for submitting code & software for further information.

Data

Policy information about availability of data

All manuscripts must include a data availability statement. This statement should provide the following information, where applicable:

- Accession codes, unique identifiers, or web links for publicly available datasets
- A list of figures that have associated raw data
- A description of any restrictions on data availability

The cryo-EM maps have been deposited in the Electron Microscopy Data Bank under EMD-21127, EMD-21128, EMD-21129, EMD-21130, EMD-21131, EMD-21537, and EMD-21538. Atomic models have been deposited in the Protein Data Bank under 6V9V, 6V9W, 6V9X, and 6V9Y.

Field-specific reporting

Please select the one below that is the best fit for your research. If you are not sure, read the appropriate sections before making your selection.

☒ Life sciences ☐ Behavioural & social sciences ☐ Ecological, evolutionary & environmental sciences

For a reference copy of the document with all sections, see nature.com/documents/nr-reporting-summary-flat.pdf

Life sciences study design

All studies must disclose on these points even when the disclosure is negative.

Sample size	No calculations were made to predetermine sample size. Sample size was chosen based on literature review, consideration of limited or rare resources, and the number of independent experiments required for strong inference of meaningful conclusions.
Data exclusions	None.
Replication	All results were successfully replicated; number of independent experiments (i.e, replicates) indicated in the text.
Randomization	Samples were not randomized; it is not technically or practically feasible to do so for cryo-EM or patch-clamp studies.
Blinding	Researchers were not blinded; it was not technically or practically feasible to do so for cryo-EM or patch-clamp studies.

Reporting for specific materials, systems and methods

We require information from authors about some types of materials, experimental systems and methods used in many studies. Here, indicate whether each material, system or method listed is relevant to your study. If you are not sure if a list item applies to your research, read the appropriate section before selecting a response.

Materials & experimental systems

n/a	Involved in the study
☒	☐ Antibodies
☐	☒ Eukaryotic cell lines
☒	☐ Palaeontology
☒	☐ Animals and other organisms
☒	☐ Human research participants
☒	☐ Clinical data

Methods

n/a	Involved in the study
☒	☐ ChIP-seq
☒	☐ Flow cytometry
☒	☐ MRI-based neuroimaging

Eukaryotic cell lines

Policy information about cell lines

Cell line source(s)	Human embryonic kidney (HEK293Tand 293F) purchased from ATCC
Authentication	Authenticated by vendor, ATCC
Mycoplasma contamination	Cell lines were certified as testing negative for Mycoplasma by the vendor, ATCC
Commonly misidentified lines (See ICLAC register)	HEK cells are listed in the register; however, the ICLAC register does not specify which strain of HEK cells. Our secondary HEK293T and F (HEK) cell lines were purchased directly from the vendor (ATCC), where they were validated. HEK cells are the only secondary cell lines used in this study. HEK cells were cultured in a dedicated secondary cell incubator free from potential contaminating primary or secondary cultures, and were used only for transient expression of ion channels for biochemical and electrophysiological studies.